The Astrophysical Journal, 900:71 (15pp), 2020 September 1 https://doi.org/10.3847/1538-4357/abab9c

Multi-frequency General Relativistic Radiation-hydrodynamics with M_1 Closure

Peter Anninos[1] and P. Chris Fragile[2]
[1] Lawrence Livermore National Laboratory, P.O. Box 808, Livermore, CA 94550, USA
[2] Department of Physics & Astronomy, College of Charleston, Charleston, SC 29424, USA; fragilep@cofc.edu
Received 2020 June 17; revised 2020 July 22; accepted 2020 July 30; published 2020 September 2

Abstract

We report on recent upgrades to our general relativistic radiation-magnetohydrodynamics code, *Cosmos++*, which expands the two-moment, $\boldsymbol{M}_1$, radiation treatment from gray to multi-frequency transport, including Doppler and gravitational frequency shifts. The solver accommodates either photon (Bose–Einstein) or neutrino (Fermi–Dirac) statistical distribution functions with absorption, emission, and elastic scattering processes. An implicit scheme is implemented to simultaneously solve the primitive inversion problem together with the radiation–matter coupling source terms, providing stability over a broad range of opacities and optical depths where the interaction terms can be stiff. We discuss our formulations and numerical methods, and validate our methods against a wide variety of test problems spanning optically thin to thick regimes in flat, weakly curved, and strongly curved spacetimes.

Unified Astronomy Thesaurus concepts: Computational methods (1965); Radiative magnetohydrodynamics (2009); Astrophysical fluid dynamics (101)

1. Introduction

Today we are living in an exciting multi-messenger era in astronomy. Telescopes cover the entire electromagnetic (EM) spectrum, with nightly full-sky coverage becoming a reality (e.g., Chambers et al. 2016; Graham et al. 2019; Ivezić et al. 2019). Additionally, cosmic-ray detectors (e.g., Cerenkov Telescope Array Consortium et al. 2019), neutrino detectors (e.g., Aartsen et al. 2019), and now gravitational wave detectors (Abbott et al. 2018) give us views of the universe beyond EM radiation, and as each new means of observation has been added, new discoveries have quickly followed (e.g., Abbott et al. 2017; Metzger 2017; IceCube Collaboration et al. 2018; Keivani et al. 2018; Fang et al. 2019). Certainly many more are to be expected.

A principal focus of multi-messenger astronomy is the transient universe (Charles & Shaw 2013), particularly events that are characterized by short bursts of electromagnetic radiation, possibly accompanied by cosmic-ray, neutrino, or gravitational wave signals, such as kilonovae (e.g., Abbott et al. 2017; Metzger 2017), fast radio bursts (e.g., Burke-Spolaor 2018; Wang et al. 2020), gamma-ray bursts (e.g., Burns et al. 2019), and tidal disruption events (e.g., Senno et al. 2017). These events are often highly energetic and commonly associated with compact objects (white dwarfs, neutron stars, or black holes), suggesting that relativistic physics plays a role.

The many new discoveries in multi-messenger astronomy need to be matched by corresponding developments in the computational tools that help in their interpretation and understanding. Over the decades, advances in observational capabilities have seen parallel developments in astrophysical simulation tools toward ever higher levels of sophistication, ranging from relatively simple hydrodynamic and *N*-body simulations to magnetohydrodynamics (MHD), radiation MHD, and beyond (see Abramowicz & Fragile 2013, for a review of relativistic code development). Most transient phenomena require some combination of relativity, hydrodynamics, magnetic fields, and radiation to be adequately modeled. Fortunately, the number of codes available for advanced radiation MHD simulations has exploded in recent years (an incomplete list includes Farris et al. 2008; Müller et al. 2010; Shibata et al. 2011; Zanotti et al. 2011; Jiang et al. 2012; Lentz et al. 2012; Sądowski et al. 2013; Zhang et al. 2013; González et al. 2015; Just et al. 2015; Tominaga et al. 2015; Kuroda et al. 2016; Skinner et al. 2019; Ryan & Dolence 2020; Weih et al. 2020). Our own contribution is the general relativistic radiation-magnetohydrodynamics code, *Cosmos++* (Anninos et al. 2005; Fragile et al. 2012, 2014), which includes a discontinuous-Galerkin variant, COSMOSDG (Anninos et al. 2017).

As ever, though, numerical simulations are only an approximation to reality. The current limitation in radiation MHD is that solving the full Boltzmann transport equation remains computationally challenging and not entirely practical in most scenarios, owing to the large number of degrees of freedom (in space and frequency) and wide range of optical depths, although new formulations have been developed for this purpose (Davis & Gammie 2020). Therefore, most codes today treat some simplified form of radiation. One common approach is to use a scheme where only the first few moments of the radiation distribution function are evolved (Thorne 1981; Shibata et al. 2011). The most basic is the flux-limited diffusion approximation (Levermore & Pomraning 1981; Pomraning 1981), which only treats the zeroth moment, meaning it retains information only about the radiation intensity and not the direction of its propagation. A two-moment scheme, such as $\boldsymbol{M}_1$ (Levermore 1984; Dubroca & Feugeas 1999; González et al. 2007), retains both the intensity and (average) direction of radiation flow, yet still closes the system of equations at a level that remains computationally reasonable. This approach has seen wide implementation in the context of black hole accretion (Sądowski et al. 2013; Fragile et al. 2014, 2018b; McKinney et al. 2014; Mishra et al. 2016; Takahashi et al. 2016), black hole–neutron-star mergers (Foucart et al. 2015, 2016b), binary neutron stars (Foucart et al. 2016a; Sekiguchi et al. 2016), core-collapse supernovae (Just et al. 2015; O'Connor 2015; Kuroda et al. 2016), and the interaction of Type I X-ray bursts with accretion disks (Fragile et al. 2018a, 2020).

Another simplification is that most relativistic radiation MHD codes today assume a frequency-integrated (or gray) opacity and evolve the radiation field with a single characteristic frequency. However, resolving the photon (or neutrino) frequency (energy),

even crudely, can be crucially important to properly modeling and understanding many transient phenomena, such as core-collapse supernovae (e.g., Janka 2012; Burrows 2013; Foglizzo et al. 2015), tidal disruption events (Dai et al. 2018), and the outbursts of black hole X-ray binaries.

This is the goal of our current work, to extend our radiation transport capabilities from a frequency-integrated (gray) approximation to a multi-frequency (equivalently multi-energy or sometimes called multi-group) method by discretizing the radiation energy and flux equations in frequency as well as space and time. As in our previous paper (Fragile et al. 2014), we adopt the $\boldsymbol{M}_1$ closure for general relativistic transport, though we have additionally developed a multi-frequency, flux-limited diffusion (with an anisotropic Eddington tensor) solver for Newtonian systems. Much of the methodology, including the formalism and numerical methods, discussed in this paper is taken from Fragile et al. (2014), and we occasionally refer the reader back to that paper for further details, particularly regarding the high-resolution shock-capturing algorithms and the primitive inversion scheme. All of those specifics are similar to what we have developed for this work, except they are applied to the radiation fields in each frequency bin separately. The primitive inversion scheme utilizes a first-order Taylor expansion of the conserved fields together with the radiation coupling terms, again similar to our previous work except here the dimension of the matrix system scales with the number of radiation bins, and the coupling to the hydrodynamics occurs after integrating each source contribution over frequency. The most significant new element that comes from frequency-dependent transport is the introduction of a source term responsible for advecting energies in frequency space as radiation propagates through gravitational fields or experiences fluid velocities that produce shifts in the photon frequencies (or neutrino energies).

As for the organization of this paper, Section 2 follows with an overview of the essential formalism and conservation equations. Section 3 discusses our numerical implementation with an emphasis on the new elements: frequency advection, closure relations, and the implicit approach for solving the coupled primitive inversion and multi-frequency radiation source terms. Section 4 reports on a series of validating test problems, and we conclude in Section 5.

Most of the equations in this paper are written in units where $G = c = 1$, although in a few places we leave in factors of c for clarity. We adopt the usual convention whereby Greek (Latin) indices refer to spacetime (spatial) coordinates and adopt a $(-,+,+,+)$ metric signature.

2. Formalism

A multi-frequency treatment of radiation transport can be derived by selecting a finite set of frequency groups (or bins) and defining the discrete energy densities $E_{(\nu)n}$ as integrals of the energy spectral densities, $E_{(\nu)}$, over the group frequency interval $\delta\nu_n$. Mathematically, $E_n = \int_{\nu_n-\delta\nu_n/2}^{\nu_n+\delta\nu_n/2} E_{(\nu)}d\nu$, and therefore $E = \sum_n E_{(\nu)n} = \int_{\nu_l}^{\nu_u} E_{(\nu)}d\nu$, where ν_l and ν_u are the lower and upper limits to our frequency bins. In this notation, the total stress-energy tensor can be written as

$$T^{\alpha\beta} = T^{\alpha\beta}_{\rm fluid} + \int d\nu \sum_i R^{\alpha\beta}_{i\ (\nu)}, \tag{1}$$

where $T^{\alpha\beta}_{\rm fluid}$ is the fluid component, and $R^{\alpha\beta}_{i\ (\nu)}$ is the spectral radiation stress tensor summed over all radiation components i representing photons or different neutrino species. For this work we consider only single species (either photon or single-flavor neutrino) transport.

The spectral radiation tensor, $R^{\alpha\beta}_{(\nu)}$, can be written in any number of ways, depending on the frame of reference. For example, the representations

$$R^{\alpha\beta}_{(\nu)} = E_{(\nu)}n^\alpha n^\beta + F^\alpha_{(\nu)}n^\beta + F^\beta_{(\nu)}n^\alpha + P^{\alpha\beta}_{(\nu)}, \tag{2}$$

$$= J_{(\nu)}u^\alpha u^\beta + H^\alpha_{(\nu)}u^\beta + H^\beta_{(\nu)}u^\alpha + L^{\alpha\beta}_{(\nu)}, \tag{3}$$

$$= \frac{4}{3}E_{R(\nu)}u^\alpha_{R(\nu)}u^\beta_{R(\nu)} + \frac{1}{3}E_{R(\nu)}g^{\alpha\beta}, \tag{4}$$

are commonly used for formalisms in the Eulerian (lab), co-moving (fluid), or isotropic (radiation) frame, respectively, where $n_\alpha = (-\alpha, 0, 0, 0)$ is a timelike vector orthogonal to the spacelike hypersurface, u^α is the fluid rest-frame 4-velocity, and $\alpha = 1/\sqrt{-g^{00}}$ is the lapse function. The quantities $E_{(\nu)}$, $J_{(\nu)}$, and $E_{R(\nu)}$ represent the frequency-dependent radiation energy densities in the different frames; likewise, $F^\alpha_{(\nu)}$ and $H^\alpha_{(\nu)}$ represent the radiation momentum densities. Finally, $P^{\alpha\beta}_{(\nu)}$ and $L^{\alpha\beta}_{(\nu)}$ are most often referred to as the pressure or stress tensors of the radiation. In previous work (Fragile et al. 2014), we adopted the radiation-frame formalism (Sądowski et al. 2013), which offers some unique advantages for computation. Notice, for example, that the radiation pressure does not appear in the isotropic stress tensor, because it implicitly represents the covariant formulation of the $\boldsymbol{M}_1$ closure scheme (Levermore 1984), which assumes the radiation is isotropic in the radiation rest frame.[3] There is also no explicit appearance of a radiation momentum density in the radiation frame. However, certain calculations are most conveniently done in either the fluid or Eulerian frame, so we retain the flexibility to transform between the different reference frames and fields. To this end, we explicitly write out here some of the more important relations between radiation fields and moments.

First, the frame-dependent primitive moments are extracted from the spectral radiation stress tensor (or equivalently the conserved or evolved radiation fields) as

$$E_{(\nu)} = R^{\alpha\beta}_{(\nu)}n_\alpha n_\beta, \quad F^i_{(\nu)} = -R^{\alpha\beta}_{(\nu)}n_\alpha\gamma^i_\beta, \quad P^{ij}_{(\nu)} = R^{\alpha\beta}_{(\nu)}\gamma^i_\alpha\gamma^j_\beta, \tag{5}$$

and

$$J_{(\nu)} = R^{\alpha\beta}_{(\nu)}u_\alpha u_\beta, \quad H^\gamma_{(\nu)} = -R^{\alpha\beta}_{(\nu)}u_\alpha h^\gamma_\beta, \quad L^{\gamma\delta}_{(\nu)} = R^{\alpha\beta}_{(\nu)}h^\gamma_\alpha h^\delta_\beta, \tag{6}$$

where $\gamma_{\alpha\beta} = g_{\alpha\beta} + n_\alpha n_\beta$ is the spatial metric, $h_{\alpha\beta} = g_{\alpha\beta} + u_\alpha u_\beta$ is the fluid-frame projection metric, and the second-rank tensors $P^{ij}_{(\nu)}$ and $L^{\gamma\delta}_{(\nu)}$ are determined by closure relations to be discussed later. Additionally we can relate the energy and flux variables directly via (Shibata et al. 2011)

$$J_{(\nu)} = E_{(\nu)}w^2 - 2wF^k_{(\nu)}u_k + P^{ij}_{(\nu)}u_iu_j, \tag{7}$$

$$H^\alpha_{(\nu)} = [E_{(\nu)}w - F^k_{(\nu)}u_k]h^\alpha_\beta n^\beta + wh^\alpha_\beta F^\beta_{(\nu)} - P^{ij}_{(\nu)}h_i{}^\alpha u_j, \tag{8}$$

[3] We are as yet unaware of any general proof of the existence of such a frame, though from our experience we have not found any cases where this formulation breaks down.

where $w = \alpha u^0$ is the Lorentz factor. The flux vector and pressure tensor in the Eulerian frame additionally satisfy $F^{\alpha}n_{\alpha} = P^{\alpha\beta}n_{\alpha} = 0$, implying $F^0_{(\nu)} = P^{0\alpha}_{(\nu)} = 0$, a fact we have exploited in writing Equations (7) and (8).

The radiation variables, $E_{R(\nu)}$ and $u^{\alpha}_{R(\nu)}$, representing the spectral radiation energy density in the radiation rest frame and the 4-velocity of the radiation rest frame itself, can easily be defined in terms of either lab- or fluid-frame tensor components. In particular, the quadratic equations

$$g_{\alpha\beta}R^{0\alpha}_{(\nu)}R^{0\beta}_{(\nu)} = -\frac{8}{9}E^2_{R(\nu)}[u^0_{R(\nu)}]^2 + \frac{1}{9}E^2_{R(\nu)}g^{00}, \tag{9}$$

$$R^{00}_{(\nu)} = \frac{4}{3}E_{R(\nu)}[u^0_{R(\nu)}]^2 + \frac{1}{3}E_{R(\nu)}g^{00}, \tag{10}$$

can be solved for $E_{R(\nu)}$ and $u^0_{R(\nu)}$ (Sądowski et al. 2013). The remaining spatial components of the radiation 4-velocity, $u^i_{R(\nu)}$, are derived from the time components of the radiation stress tensor.

Following the truncated moment formalism (Thorne 1981; Shibata et al. 2011), the radiation conservation equations become

$$R^{\alpha\beta}_{(\nu);\beta} - \frac{\partial}{\partial\nu}[\nu M^{\alpha\beta\gamma}_{(\nu)}u_{\beta;\gamma}] = -G_{\alpha(\nu)}, \tag{11}$$

where $G_{\alpha(\nu)}$ represents radiation–matter interaction source terms, and $M^{\alpha\beta\gamma}_{(\nu)}$ is the third-rank moment tensor associated with Doppler and gravitational frequency shifts.

These radiation equations are solved together with the conservation equations for mass $(\rho u^{\beta})_{;\beta} = 0$ and fluid stress-energy $(T^{\beta}_{\alpha})_{;\beta} = \int G_{\alpha(\nu)}d\nu$. Ignoring non-ideal effects and magnetic fields, the fluid stress-energy tensor takes the form

$$T^{\alpha\beta} = (\rho + \rho\epsilon + P_{\rm gas})u^{\alpha}u^{\beta} + P_{\rm gas}g^{\alpha\beta}, \tag{12}$$

where $P_{\rm gas}$ is the gas pressure. Although we do not consider magnetic fields or viscosity in this work, we advertise that both of these physics capabilities are currently fully integrated with this multi-frequency radiation upgrade. We refer the reader to Fragile et al. (2012, 2018b) for details of their respective implementations.

Coupling of the fluid and radiation equations occurs through the radiation 4-force density, $G^{\mu}_{(\nu)}$, written in the form

$$G^{\mu}_{(\nu)} = -\rho[\kappa^{\rm a}_{(\nu)} + \kappa^{\rm s}_{(\nu)}]R^{\mu\nu}_{(\nu)}u_{\nu} - \rho[\kappa^{\rm s}_{(\nu)}R^{\alpha\beta}_{(\nu)}u_{\alpha}u_{\beta} + \kappa^{\rm a}_{(\nu)}B_{(\nu)}]u^{\mu}, \tag{13}$$

where $\kappa^{\rm a}_{(\nu)}$ and $\kappa^{\rm s}_{(\nu)}$ represent the frequency-dependent absorption/emission and elastic scattering opacities, respectively; $B_{(\nu)}$ is the Bose–Einstein or Fermi–Dirac statistical distribution function

$$B_{(\nu)} = \frac{4\pi g(h\nu)^3}{(hc)^3}\left(\frac{1}{e^{(h\nu-\mu_{\nu})/(kT)} - \eta}\right), \tag{14}$$

where μ_{ν} is the chemical potential, $g = 2$ (1) is the statistical weight for photons (neutrinos), and $\eta = 1$ (−1) for photons (neutrinos). The gray (frequency-integrated) version of Equation (13) can be written as

$$G^{\mu} = -\rho(\kappa^{\rm a}_{\rm F} + \kappa^{\rm s})R^{\mu\nu}u_{\nu} - \rho[(\kappa^{\rm s} + \kappa^{\rm a}_{\rm F} - \kappa^{\rm a}_{\rm A})R^{\alpha\beta}u_{\alpha}u_{\beta} + \kappa^{\rm a}_{\rm P}a_R T^4]u^{\mu}, \tag{15}$$

where a_R is the radiation constant (different for photons and neutrinos) and $\kappa^{\rm a}_{\rm F}$, $\kappa^{\rm a}_{\rm A}$, and $\kappa^{\rm a}_{\rm P}$ are the flux, absorption, and Planck mean opacities, respectively.

Expanding out the covariant derivatives, the full set of conservation equations to be solved are written as

$$\partial_t D + \partial_i(DV^i) = 0, \tag{16}$$

$$\partial_t\mathcal{E} + \partial_i(-\sqrt{-g}\ T^i_0) = -\sqrt{-g}\ T^{\alpha}_{\beta}\ \Gamma^{\beta}_{0\alpha} - \sqrt{-g}\ G_0, \tag{17}$$

$$\partial_t\mathcal{S}_j + \partial_i(\sqrt{-g}\ T^i_j) = \sqrt{-g}\ T^{\alpha}_{\beta}\ \Gamma^{\beta}_{j\alpha} + \sqrt{-g}\ G_j, \tag{18}$$

$$\partial_t\mathcal{R}_{(\nu)} + \partial_i[-\sqrt{-g}\ R^i_{0(\nu)}] = -\frac{\partial}{\partial\nu}[\nu M_{0\beta\gamma(\nu)}u^{\beta;\gamma}] - \sqrt{-g}\ R^{\alpha}_{\beta(\nu)}\ \Gamma^{\beta}_{0\alpha} + \sqrt{-g}\ G_{0(\nu)}, \tag{19}$$

$$\partial_t\mathcal{R}_{j(\nu)} + \partial_i[\sqrt{-g}\ R^i_{j(\nu)}] = \frac{\partial}{\partial\nu}[\nu M_{j\beta\gamma(\nu)}u^{\beta;\gamma}] + \sqrt{-g}\ R^{\alpha}_{\beta(\nu)}\ \Gamma^{\beta}_{j\alpha} - \sqrt{-g}\ G_{j(\nu)}, \tag{20}$$

where $D = W\rho$, ρ is the rest-frame fluid density, $W = \sqrt{-g}u^0 = \sqrt{-g}(\gamma/\alpha)$ is the relativistic boost factor, $V^i = u^i/u^0$ is the fluid transport velocity, g is the 4-metric determinant, $\Gamma^{\beta}_{\alpha\gamma}$ are the geometric connection coefficients of the metric, $\mathcal{E} = -\sqrt{-g}\,T^0_0$ is the total energy density, $\mathcal{S}_j = \sqrt{-g}\,T^0_j$ is the covariant momentum density, $\mathcal{R}_{(\nu)} = -\sqrt{-g}\,R^0_{0(\nu)}$ is the conserved radiation spectral energy, $\mathcal{R}_{j(\nu)} = \sqrt{-g}\,R^0_{j(\nu)}$ is the conserved radiation spectral momentum, and $G_{\alpha} = \int G_{\alpha(\nu)}d\nu$.

3. Numerical Implementation

Equations (16)–(20) are solved by operator splitting terms into spacetime advection, curvature, frequency advection, and radiation–matter coupling. The first three contributions are solved using high-order explicit methods, while the fourth is updated with a fully implicit approach, which provides stability when radiation–matter interactions become stiff relative to a hydrodynamic timescale, as they often do when strongly coupled. Solution methods for each of these contributions are discussed below.

3.1. Advection and Curvature

The radiation conservation laws (19) and (20) are identical in form to the equations for fluid energy and momentum conservation already solved in *Cosmos++*, and are amenable to similar numerical techniques, specifically the high-resolution shock-capturing (HRSC) scheme as described in Fragile et al. (2012).

Representing conserved fields as $\boldsymbol{U} = [D, \mathcal{E}, \mathcal{S}_j, \mathcal{R}_{(\nu)}, \mathcal{R}_{j(\nu)}]$, the discrete finite-volume representation of Equations (16)–(20) is written in generic fashion as

$$\boldsymbol{U}^* = \boldsymbol{U}^n - \frac{\Delta t}{V}\sum_{\text{cell faces}}(\boldsymbol{F}^i A_i)^n + \Delta t\ \boldsymbol{S}^n_c, \tag{21}$$

where $\boldsymbol{S}_c(\boldsymbol{P})$ contains the curvature source terms, $\boldsymbol{F}^i(\boldsymbol{P}) = \sqrt{-g}\,[\rho u^0, -T^i_0, T^i_j, -R^i_{0(\nu)}, R^i_{j(\nu)}]$ are the fluxes, and $\boldsymbol{U}^*$ represents the intermediate solution state (accounting for

advection and curvature, but not frequency shift or coupling terms). Notice that both the flux and curvature source terms are computed from the set of primitive, not conserved, fields.

One of the differences between this work and that presented in Fragile et al. (2014) is the choice of primitive fields. Here we have opted to use the fluid and spectral radiation 4-velocities [u^i and $u^i_{R(\nu)}$] and not the normal observer-projected 4-velocities ($\tilde{u}^i = u^i - u^0 g^{0i}/g^{00}$) that we used previously. With this change, the set of primitive variables becomes $\boldsymbol{P} = [\rho, \epsilon, u^i, E_{R(\nu)}, u^i_{R(\nu)}]$, where ϵ is the specific internal energy as measured in the fluid rest frame.

The flux terms are calculated at zone faces using either the Harten–Lax–van Leer (HLL) or Lax–Friedrichs (LF) Riemann solver with options for linear or piecewise parabolic method (PPM) slope-limited reconstruction of the primitive fields. For the HLL solver this takes the form

$$\boldsymbol{F}_{\rm HLL} = \frac{\lambda_+ \boldsymbol{F}_{\rm L} - \lambda_- \boldsymbol{F}_{\rm R} + \lambda_- \lambda_+ (\boldsymbol{U}_{\rm R} - \boldsymbol{U}_{\rm L})}{\lambda_+ - \lambda_-}, \tag{22}$$

where R (L) subscripts denote right (left) reconstructed states, and λ_+ (λ_-) is the characteristic maximum (minimum) wave speed.

One of the advantages of formulating radiation transport in terms of the primitive radiation variables, $E_{\rm R}$ and $u^i_{\rm R}$, is that it simplifies the calculation of characteristic radiation wave speeds required for the Riemann solvers. We generally follow the prescription outlined in our gray treatment (Fragile et al. 2012) where we effectively replace the fluid velocity with the radiation velocity in the co-moving dispersion relation (Gammie et al. 2003) (see also McKinney et al. 2014)

$$\left[1 - v_T^2\left(1 + \frac{g^{00}}{u^0 u^0}\right)\right](c^i)^2 + 2\left[v_T^2\left(V^i + \frac{g^{0i}}{u^0 u^0}\right) - V^i\right]c^i + \left[V^i V^i - v_T^2\left(V^i V^i + \frac{g^{ii}}{u^0 u^0}\right)\right] = 0, \tag{23}$$

where c^i is the wave speed along each coordinate direction, x^i, and v_T is the maximum of the fluid or radiation wave speeds ($1/\sqrt{3}$ in the optically thin regime). The minimum (λ_-) and maximum (λ_+) speeds are defined by the minimum and maximum solutions of the quadratic Equation (23). Generalization to the optically thick regime is accommodated by limiting the characteristic velocities as

$$\lambda_- \rightarrow \max\left(\lambda_-, -\frac{4}{3\tau}\right) \tag{24}$$

$$\lambda_+ \rightarrow \min\left(\lambda_+, \frac{4}{3\tau}\right), \tag{25}$$

where τ is the total optical depth in the cell. Although it appears to make little difference, we provide an alternative extension of the wave speed into the optically thick regime by using the fluid-frame moments and the limiting procedure described in Section 3.2 to interpolate between the two:

$$\lambda_\pm = \frac{3\chi - 1}{2}\lambda_{\pm,\rm thin} + \frac{3(1-\chi)}{2}\lambda_{\pm,\rm thick}, \tag{26}$$

where $\lambda_{\pm,\rm thin}$ and $\lambda_{\pm,\rm thick}$ are the corresponding speeds in the optically thin and thick regimes respectively.

Advection and curvature operators are completed (advanced) with several available time discretization options. *Cosmos++* supports numerous options designed to enhance stability and accuracy for specific applications and algorithms, including (up to) fourth-order strong-stability-preserving Runge–Kutta methods that benefit high-order finite elements (Anninos et al. 2017), and multi-step Crank–Nicholson methods that stabilize highly dynamical black hole spacetimes. For the test problems presented in this report we typically use a more conventional second-order time discretization based on a low-storage forward Euler method.

3.2. Doppler and Gravitational Frequency Shifts

The frequency advection source terms are updated following the general procedure outlined in Shibata et al. (2011) (see also Kuroda et al. 2016), after transforming the radiation-frame moments to their lab-frame counterparts using Equation (5). The conservation equations for the lab-frame moments take the form

$$\partial_t E_{(\nu)} = -\frac{\partial}{\partial \nu}[\nu n_\alpha M^{\alpha\beta\gamma}_{(\nu)} u_{\beta;\gamma}], \tag{27}$$

$$\partial_t F_{j(\nu)} = \frac{\partial}{\partial \nu}[\nu \gamma_{j\alpha} M^{\alpha\beta\gamma}_{(\nu)} u_{\beta;\gamma}], \tag{28}$$

where

$$M^{\alpha\beta\gamma}_{(\nu)} u_{\gamma;\beta} = [H^\gamma_{(\nu)} u^\alpha u^\beta + L^{\alpha\gamma}_{(\nu)} u^\beta + L^{\beta\gamma}_{(\nu)} u^\alpha + N^{\alpha\beta\gamma}_{(\nu)}] u_{\gamma;\beta}, \tag{29}$$

and $N^{\alpha\beta\gamma}_{(\nu)}$ is determined by a closure formulation connecting optically thin and thick regimes,

$$N^{\alpha\beta\gamma}_{(\nu)} = \frac{3\chi - 1}{2}[N^{\alpha\beta\gamma}_{(\nu)}]_{\rm thin} + \frac{3(1-\chi)}{2}[N^{\alpha\beta\gamma}_{(\nu)}]_{\rm thick}. \tag{30}$$

We adopt the thin/thick expressions recommended in Shibata et al. (2011):

$$[N^{\alpha\beta\gamma}_{(\nu)}]_{\rm thin} = \frac{J_{(\nu)} H^\alpha_{(\nu)} H^\beta_{(\nu)} H^\gamma_{(\nu)}}{(h_{\alpha\beta} H^\alpha_{(\nu)} H^\beta_{(\nu)})^{3/2}} \tag{31}$$

and

$$[N^{\alpha\beta\gamma}_{(\nu)}]_{\rm thick} = \frac{1}{5}[H^\alpha_{(\nu)} h^{\beta\gamma} + H^\beta_{(\nu)} h^{\alpha\gamma} + H^\gamma_{(\nu)} h^{\alpha\beta}]. \tag{32}$$

Among the many options for the closure function, χ, we have chosen to use (Levermore 1984)

$$\chi = \frac{3 + 4\xi^2}{5 + 2\sqrt{4 - 3\xi^2}}, \tag{33}$$

where

$$\xi^2 = \frac{h_{\alpha\beta} H^\alpha_{(\nu)} H^\beta_{(\nu)}}{J^2_{(\nu)}} \tag{34}$$

works well as an indicator of whether the fluid is locally optically thick ($\xi \rightarrow 0$) or thin ($\xi \rightarrow 1$).

The form of Equations (27) and (28) is advective in nature and fully conservative when the boundary conditions enforce zero radiation flux at the edges of the frequency domain. We thus discretize and update both equations using a conservative multi-stage, second-order upwind scheme where the flux terms

are reconstructed at group boundaries using a minmod limiter to preserve monotonicity in the gradient extrapolants. The scheme is multi-stage in the sense that we subcycle the source update, respecting the characteristic advection time for the most rapidly changing bin energies. In particular, the subcycle time step is determined by the minimum advection time over all groups based on the covariant divergence of the fluid 4-velocity, $\delta t_{\rm sub} = \min[C_{\rm cfl}\delta\nu/(\nu|u^{\alpha}_{;\alpha}|)]$, where $C_{\rm cfl} < 1$ is a Courant factor typically set to 0.3. After advancing the lab-frame moments with Equations (27) and (28), the evolved radiation fields are easily reconstructed from the radiation stress-energy tensor (4) along with the following general relativistic $\boldsymbol{M}_1$ closure relation for the pressure:

$$P^{ij}_{(\nu)} = \frac{3\chi - 1}{2}[P^{ij}_{(\nu)}]_{\rm thin} + \frac{3(1-\chi)}{2}[P^{ij}_{(\nu)}]_{\rm thick}, \tag{35}$$

where

$$[P_{(\nu)}]^{ij}_{\rm thin} = E_{(\nu)}\frac{F^i_{(\nu)}F^j_{(\nu)}}{\gamma_{ij}F^i_{(\nu)}F^j_{(\nu)}}, \tag{36}$$

and $[P_{(\nu)}]^{ij}_{\rm thick} = E_{(\nu)}\gamma^{ij}/3$.

3.3. Primitive Inversion and Radiation–Matter Coupling

The radiation–matter coupling terms are updated using an implicit, iterative Newton–Raphson method to provide greater stability in strongly coupled regimes. In this section, we will use the index n to indicate steps or cycles in the global time-stepping scheme, whereas the index m indicates iteration steps within the Newton–Raphson solver. Once all explicit steps have been advanced, the implicit solve follows according to

$$\boldsymbol{U}^{n+1} = \boldsymbol{U}^* + \Delta t\, \boldsymbol{S}_r^{n+1}, \tag{37}$$

where $\boldsymbol{S}_r(\boldsymbol{P})^{n+1} = \sqrt{-g}\,[0, -G_0, G_j, G_{0(\nu)}, -G_{j(\nu)}]^{n+1}$ represents the interactions terms at the advanced time $n+1$. Taking the first-order Taylor expansion with respect to primitive variables, the $(m+1)$th iterate is approximated as

$$\boldsymbol{U}^{m+1} = \boldsymbol{U}^m + \sum_a \left(\frac{\partial \boldsymbol{U}}{\partial P^a}\right)^m \delta P^a \tag{38}$$

$$G^{m+1}_{\alpha} = G^m_{\alpha} + \sum_a \left(\frac{\partial G_{\alpha}}{\partial P^a}\right)^m \delta P^a, \tag{39}$$

where

$$\delta\boldsymbol{P} = \begin{pmatrix} \delta\rho \\ \delta\epsilon \\ \delta u^i \\ \delta E_{R(\nu)} \\ \delta u^i_{R(\nu)} \end{pmatrix} = \begin{pmatrix} \rho^{m+1} - \rho^m \\ \epsilon^{m+1} - \epsilon^m \\ (u^i)^{m+1} - (u^i)^m \\ E^{m+1}_{R(\nu)} - E^m_{R(\nu)} \\ [u^i_{R(\nu)}]^{m+1} - [u^i_{R(\nu)}]^m \end{pmatrix}. \tag{40}$$

Plugging the expanded form of each variable into Equation (37), we get the following set of equations for the primitive fields δP^a:

$$\sum_a \left(\frac{\partial \boldsymbol{U}^m}{\partial P^a} - \Delta t\,\frac{\partial \boldsymbol{S}^m_r}{\partial P^a}\right)\delta P^a = \boldsymbol{U}^* - (\boldsymbol{U}^m - \Delta t\,\boldsymbol{S}^m_r), \tag{41}$$

which is in linear matrix form $\boldsymbol{A}\boldsymbol{x} = \boldsymbol{b}$ with Jacobian

$$A_{ba} = \frac{\partial U^b}{\partial P^a} - \Delta t\,\frac{\partial S^b_r}{\partial P^a}, \tag{42}$$

or more explicitly

$$\boldsymbol{A} = \begin{pmatrix} \frac{\partial D}{\partial \rho} & 0 & \frac{\partial D}{\partial u^i} & 0 & 0 \\ \frac{\partial \mathcal{E}}{\partial \rho} + \Delta t\sqrt{-g}\frac{\partial G_0}{\partial \rho} & \frac{\partial \mathcal{E}}{\partial \epsilon} + \Delta t\sqrt{-g}\frac{\partial G_0}{\partial \epsilon} & \frac{\partial \mathcal{E}}{\partial u^i} + \Delta t\sqrt{-g}\frac{\partial G_0}{\partial u^i} & \Delta t\sqrt{-g}\frac{\partial G_0}{\partial E_R} & \Delta t\sqrt{-g}\frac{\partial G_0}{\partial u^i_R} \\ \frac{\partial \mathcal{S}_j}{\partial \rho} - \Delta t\sqrt{-g}\frac{\partial G_j}{\partial \rho} & \frac{\partial \mathcal{S}_j}{\partial \epsilon} - \Delta t\sqrt{-g}\frac{\partial G_j}{\partial \epsilon} & \frac{\partial \mathcal{S}_j}{\partial u^i} - \Delta t\sqrt{-g}\frac{\partial G_j}{\partial u^i} & -\Delta t\sqrt{-g}\frac{\partial G_j}{\partial E_R} & -\Delta t\sqrt{-g}\frac{\partial G_j}{\partial u^i_R} \\ -\Delta t\sqrt{-g}\frac{\partial G_0}{\partial \rho} & -\Delta t\sqrt{-g}\frac{\partial G_0}{\partial \epsilon} & -\Delta t\sqrt{-g}\frac{\partial G_0}{\partial u^i} & \frac{\partial \mathcal{R}}{\partial E_R} - \Delta t\sqrt{-g}\frac{\partial G_0}{\partial E_R} & \frac{\partial \mathcal{R}}{\partial u^i_R} - \Delta t\sqrt{-g}\frac{\partial G_0}{\partial u^i_R} \\ \Delta t\sqrt{-g}\frac{\partial G_j}{\partial \rho} & \Delta t\sqrt{-g}\frac{\partial G_j}{\partial \epsilon} & \Delta t\sqrt{-g}\frac{\partial G_j}{\partial u^i} & \frac{\partial \mathcal{R}_j}{\partial E_R} + \Delta t\sqrt{-g}\frac{\partial G_j}{\partial E_R} & \frac{\partial \mathcal{R}_j}{\partial u^i_R} + \Delta t\sqrt{-g}\frac{\partial G_j}{\partial u^i_R} \end{pmatrix}, \tag{43}$$

and

$$\boldsymbol{b} = \boldsymbol{U}^* - (\boldsymbol{U}^m - \Delta t\,\boldsymbol{S}^m_r) = \begin{pmatrix} D^* - D^m \\ \mathcal{E}^* - \mathcal{E}^m - \Delta t\sqrt{-g}\,G^m_0 \\ \mathcal{S}^*_j - \mathcal{S}^m_j + \Delta t\sqrt{-g}\,G^m_j \\ \mathcal{R}^*_{(\nu)} - \mathcal{R}^m_{(\nu)} + \Delta t\sqrt{-g}\,G^m_{0(\nu)} \\ \mathcal{R}^*_{j(\nu)} - \mathcal{R}^m_{j(\nu)} - \Delta t\sqrt{-g}\,G^m_{j(\nu)} \end{pmatrix}. \tag{44}$$

Notice that $\boldsymbol{A}$ is really a matrix of size $(5+4N_B)\times(5+4N_B)$, and $\boldsymbol{x}$ and $\boldsymbol{b}$ are $(5+4N_B)$-dimensional vectors, where N_B is the number of frequency bins; we have simply condensed the notation by representing each 3-vector and all spectral components in $\boldsymbol{A}$, $\boldsymbol{x}$, and $\boldsymbol{b}$ as single entries. The linear system only includes terms known at iteration m. From these we can solve for the vector of unknown primitives at iteration $m+1$, $\boldsymbol{P}^{m+1} = \boldsymbol{P}^m + \boldsymbol{x}$, by inverting the matrix $\boldsymbol{A}$, solving for $\boldsymbol{x}$, then repeating until $\delta\boldsymbol{P}/\boldsymbol{P}$ converges to a specified tolerance, which we typically set to $< 10^{-5}$ for all primitive fields.

In addition to this analytic approach we have also developed a numerical method for calculating the Jacobian matrix that is based on a forward difference approximation to the derivatives, in which all conserved fields and source terms are evaluated as functions of the primitive iterates. We have tested both analytic and numerical procedures for calculating the derivatives in (43). Both produce consistent results, but we currently use the

analytic method as our primary (default) option because it is faster. The Appendix summarizes all of the derivative expressions needed for calculating $\boldsymbol{A}$ analytically.

While this approach is limited to first-order accuracy in time whenever the radiation source terms are stiff (i.e., for large optical depths), it does have the advantages that it: (1) is relatively easy to implement; (2) is stable over a much broader range of parameters than a fully explicit scheme (see Fragile et al. 2014); and (3) is asymptotic preserving (Pareschi & Russo 2001). In future work, we plan to look into implementing higher-order implicit–explicit (IMEX) schemes. This strategy for solving the radiation source terms also clearly accomplishes the primitive inversion step, since we ultimately end up with the set of primitives $\boldsymbol{P}$ at the new time step $n+1$. The difference from radiation coupling is that it introduces elements into the Jacobian matrix that depend on the time step, so care must be taken in how, when, and how often this operation is performed in the time sequence.

4. Test Problems

The Courant factor is set to $k_{\rm CFL}=0.1$ for all problems, except for the radiation shock tube cases ($k_{\rm CFL}=0.3$) and the free-streaming wave front test ($k_{\rm CFL}=0.2$). The primitive solver tolerance is set to 10^{-5}, except for the radiation shock tubes, which use 10^{-8}. All calculations use the closure functions (33) and (34) of Levermore (1984). Unless otherwise noted, the radiation energy is plotted in the Eulerian (lab) frame.

4.1. Free-streaming Wave Front

An important advantage of the $\boldsymbol{M}_1$ closure method is its ability to capture the free-streaming limit much more accurately than an energy diffusion scheme, even with the steepest flux limiters. So this is an appropriate problem with which to begin testing because it is also the simplest to validate. For this test, we set a background gas with $\rho=1\,{\rm g\,cm^{-3}}$, $T=10^4$ K, and $\kappa=1$ cm^2 g^{-1}. We then heat the left boundary to a temperature of 10^6 K and set the initial radiation energy to $E=a_rT^4$ and radiation flux to $F=0.999cE$. The entire grid length is fixed at 0.01 of a mean free path so the medium remains optically thin to photons throughout their propagation history. We assume a constant opacity in temperature, density, and frequency, but we nevertheless run this test with multiple frequency groups (three), assigning spectral energies $E_{(\nu)n}=[E/(h\delta\nu_n)]/N_b$ and spectral fluxes $F_{(\nu)n}=cE_{(\nu)n}$, where $\delta\nu_n$ is the width of bin n and $N_b=3$ is the number of frequency bins. The bins are spaced logarithmically from 10^{-2} to 10^4 eV. Figure 1 plots the three spectral energy densities together with the analytic solution for the total energy density (normalized such that $E=\int E_{(\nu)}d\nu=1$ behind the wave front) after the wave front has traveled roughly 70% of the grid length. Note that the spectral energy densities, $E_{(\nu)n}$, are in units of energy density per energy $[E/(h\delta\nu)]$, so they are shifted in amplitude from the analytic solution, which is just an energy density, by the different spectral bin widths (and number of bins). We intentionally plotted it this way to separate out the energy density profiles for clarity. It is easy to confirm, however, that $E_{(\nu)1}\delta\nu_1+E_{(\nu)2}\delta\nu_2+E_{(\nu)3}\delta\nu_3\approx E$. We observe a slight overshoot in $E_{(\nu)n}$ of roughly 10%–15% at the front edge of the wave, but otherwise the numerical and analytic solutions

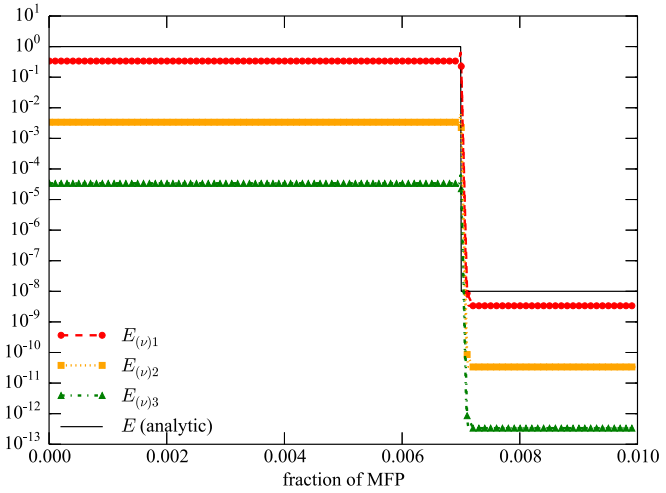

Figure 1. Binned spectral energy densities, $E_{(\nu)n}$, and the analytic frequency-integrated energy density, E, for the free-streaming wave problem. Note that the units of $E_{(\nu)n}$ are energy density per energy, while the units of E are just energy density. The horizontal axis is in units of the photon mean free path (MFP) for this problem.

agree quite nicely. The average relative error, $\sum_i|a_i-A_i|/(NA_i)$, where a_i and A_i are the numerical and analytic solutions, respectively, of E is $<8\times10^{-3}$ for $N=1000$ zones, and converges at a rate slightly faster than first order, as expected for problems with sharp discontinuities.

4.2. Diffusive Point Source

In the opposite, optically thick limit, Pons et al. (2000) proposed an analytically tractable problem describing the propagation of a single point source in a strongly diffusive medium. The medium is endowed with zero absorptivity but very high scattering opacity in each frequency bin $\kappa^s_{(\nu)}$. For a sufficiently opaque, spherically symmetric medium, the lab-frame energy and flux evolve as a function of radius (r) and time (t) according to

$$E(r,t)=\left(\frac{k_s}{t}\right)^{3/2}\exp\left(\frac{-3k_sr^2}{4ct}\right), \tag{45}$$

$$F^r(r,t)=\frac{r}{2t}E. \tag{46}$$

The tests presented here fix the grid length to $R=2\times10^9$ cm, the gas density to $\rho_0=9\times10^{14}\,{\rm g\,cm^{-3}}$, and the gas temperature to 5×10^6 eV. Specification of the Péclet number $P_e=\kappa_s\Delta\ell$, where $\Delta\ell$ is a characteristic scale, defines the scattering opacity. We tie the length scale to a small fraction of the grid length $\Delta\ell=R/50$ and set $P_e=100$, safely within the strong scattering limit. All calculations are initialized at $t_0=200R/c$, and for the convergence studies they run out to $t=1.5t_0$, enough time for the solutions to decay to roughly half of their initial peak energies. Similar to the streaming test, these problems are run with three logarithmically spaced spectral bins ranging from 10^4 to 10^8 eV and initialized with spectral energy densities $E_{(\nu)}$ and fluxes $F^r_{(\nu)}$ such that the frequency-integrated lab-frame energy density and flux equate to Equations (45) and (46). Results for $E(r)$ on a grid with $N=200$ zones are plotted in Figure 2. We find average (maximum) errors of E of 2.3×10^{-3} (8.7×10^{-3}) and

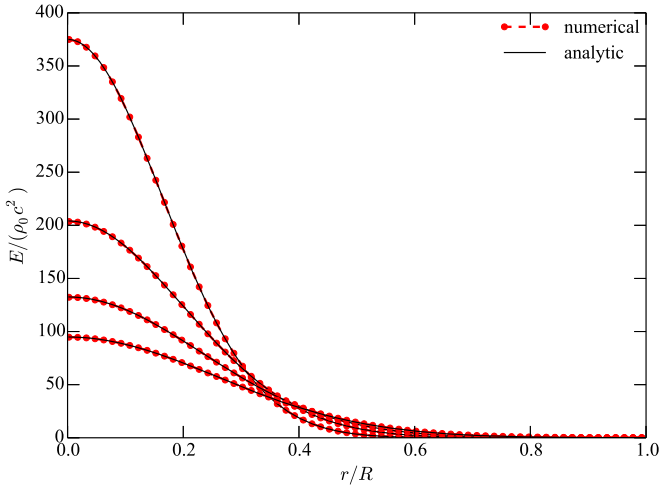

Figure 2. Frequency-integrated radiation energy density for the diffusive point source test, calculated on a grid of 200 zones at times $t = 200$, 300, 400, and 500. The numerical solution converges at second order toward the analytic solution.

5.9×10^{-4} (2.6×10^{-3}) on grids of $N = 100$ and 200 zones, respectively, consistent with a second-order convergence rate.

4.3. Picket Fence

Analytic benchmark solutions for non-equilibrium radiative transfer are scarce, and this is especially true for multi-frequency general relativistic transfer. Hence we occasionally resort, as we do in this section, to the Newtonian literature and limit. As we have emphasized, the radiative transfer algorithms in *Cosmos++* are adapted to work in both Newtonian and general relativistic regimes, and because of the covariant nature of the formalism, much of the coding is shared. In fact the only major difference between the two is the primitive inversion scheme, which is not needed for the Newtonian limit. As a result Newtonian problems will exercise much of the general relativistic coding.

One particularly interesting Newtonian problem is the picket fence proposed by Su & Olson (1999). This test provides a semianalytic solution for non-gray, two-temperature, non-equilibrium radiative transfer and diffusion, with the caveats that the opacity must be independent of temperature and the material specific heat must be proportional to the cube of the temperature, i.e., $C_v = \alpha T^3$. This problem is initialized with a cold, purely absorbing medium, then heated by an extended isotropic radiation source that is a function of space, time, and frequency $S(x, t, \nu)$. The source is actually constant over space and time, but active only for a finite duration and over a finite region of space. Hydrodynamic motion (other than thermal coupling) is ignored.

The cold medium is initialized with unit density, unit temperature, and specific heat constant $\alpha = 4a_r/\epsilon$, where a_r is the radiation constant and $\epsilon = 1$. The multi-frequency aspect of this test is scripted in the opacity, which is assumed to take one of two values, $\kappa(\nu) = \kappa_n$ where $n = (1, 2)$, across alternating frequency bins. We use 20 bins to cover (logarithmically) the frequency range 10^{-8}–10 eV$/h$, and set the alternating opacities to 2 and 20. The radiating source emits at the rate $S = ca_r\rho\kappa_0 T_0^4$ erg s^{-1} cm^{-3}, where $T_0 = 10^3$ K and $\kappa_0 = (\kappa_1 + \kappa_2)/2$ is the mean opacity, corresponding to Case

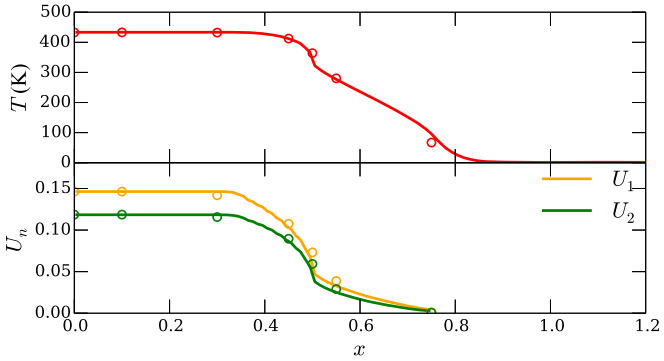

Figure 3. Temperature (top panel) and frequency-integrated radiation energy densities (bottom panel) for the picket-fence test Case $\mathscr{B}$ from Su & Olson (1999) at $\tau = 0.3$ run on a grid of 300 zones. The analytic transport solutions are included as symbols.

$\mathscr{B}$ from Su & Olson (1999). The numerical box size is set to three mean free paths and the radiating source is contained within half a mean free path of the leftmost edge of the grid. Figure 3 plots the results at $\tau = 0.3$, where τ is the time measured in units of $\alpha/(4ca_r\rho\kappa_0)$. The upper panel presents the gas temperature, while the lower panel shows the radiation energies corresponding to the quantities U_1 and U_2 in the notation of Su & Olson (1999), which represent the total integrated energies across each of the two opacity intervals, i.e., $U_n = \int E_{(\nu)n} d\nu_n$. We also include the benchmark transport solutions as tabulated in Su & Olson (1999). The agreement with the numerical solutions is better than 10% throughout the temperature and energy profiles, a fairly good agreement considering that the $\boldsymbol{M}_1$ closure makes different assumptions than the transport model.

4.4. Homogeneous Radiating Sphere

We next consider two variants of the homogeneous radiating sphere test (Müller et al. 2010). The basic configuration consists of a static, spherically symmetric, homogeneous, and isothermal stellar sphere of radius $R_\star$, which radiates into a surrounding vacuum region. We assume that the dominant interaction process inside the sphere is isotropic absorption and thermal emission with constant absorption opacity $\kappa^a_{(\nu)}$ and emissivity B. Under such conditions, this problem has the following analytic solution (Smit et al. 1997):

$$I(r, \mu) = B(1 - e^{-\kappa s(r,\mu)}), \tag{47}$$

where

$$s(r, \mu) = \begin{cases} r\mu + R_\star g(r, \mu) & \text{if } r < R_\star, \quad -1 \leqslant \mu \leqslant 1, \\ 2R_\star g(r, \mu) & \text{if } r \geqslant R_\star, \quad \sqrt{1 - (R_\star/r)^2} \leqslant \mu \leqslant 1, \\ 0, & \text{otherwise}, \end{cases} \tag{48}$$

$$g(r, \mu) = \sqrt{1 - \left(\frac{r}{R_\star}\right)^2 (1 - \mu^2)}, \tag{49}$$

and $\mu = \cos\theta$ is the directional cosine, such that this solution is an integral over all directions. The radiation energy and flux are derived via a numerical integration of the first two moments (angular integrals) of (47).

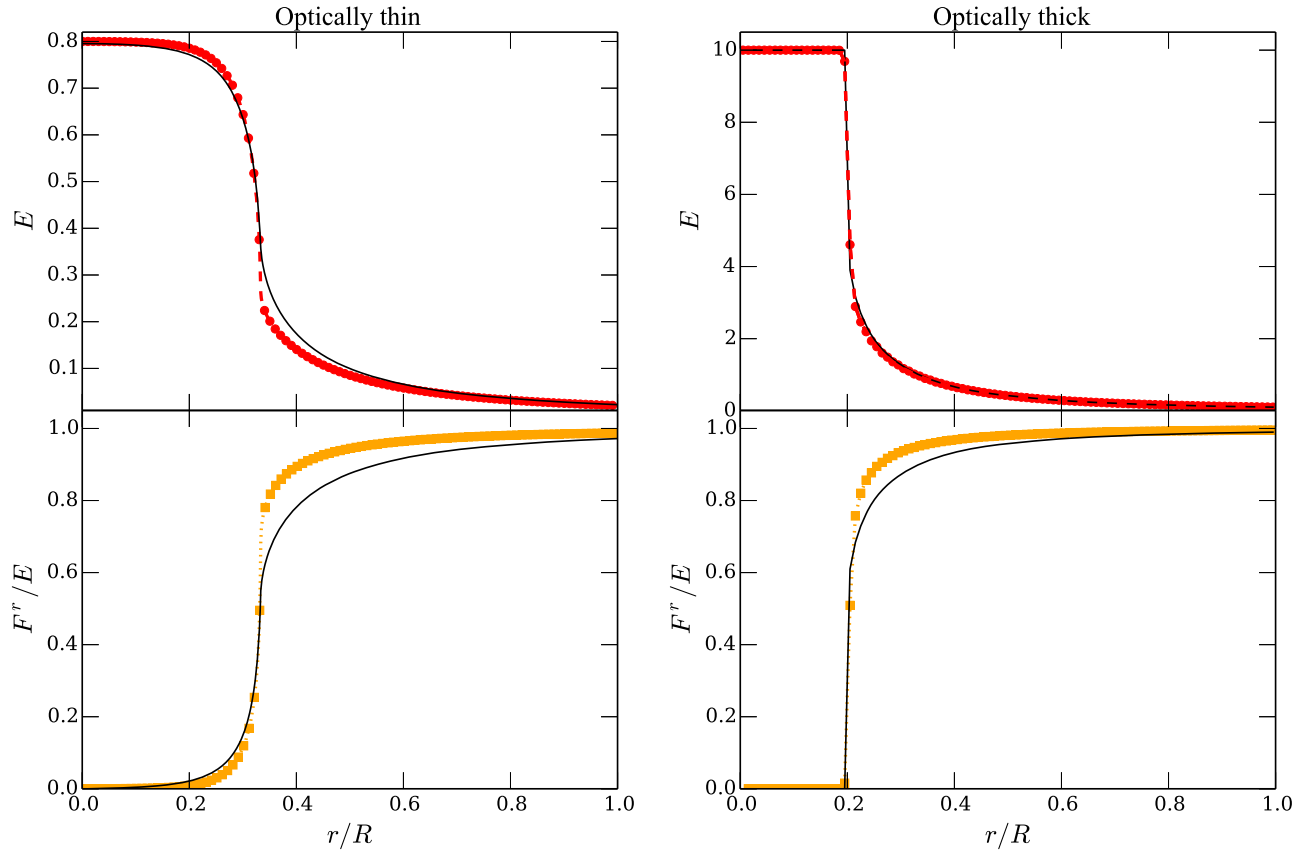

Figure 4. Steady-state radiation energy densities (top panels) and radial flux ratios (bottom panels) for the homogeneous radiating sphere tests. The left (right) panels are the optically thinner (thicker) solutions. Symbols show the numerical solutions, while the thin black lines give the analytic ones.

We set the sphere radius to $R_\star = 10$ km and initialize the interior with a constant density $\rho_0 = 9 \times 10^{14}\,\mathrm{g\,cm^{-3}}$, a constant temperature with the parameterization $T_0 = (B/a_r)^{1/4}$, and opacity $\kappa = P_e/\Delta r$ where $\Delta r = R/N_r$ is the cell size, R is the grid domain length, N_r is the number of grid cells, and P_e is the Péclet number. The exterior background density is fixed at $10^{-10}\rho_0$. We consider two parameter sets representing different optical regimes: an optically thinner case (Smit et al. 1997) with $N_r = 1000$, $R = 3R_\star$, $B = 0.8$, and $P_e = 0.015$, and a very thick case (Abdikamalov et al. 2012) with $N_r = 100$, $R = 5R_\star$, $B = 10$, and $P_e = 12.5$. The steady-state solutions for the radiation energies and ratios of radial flux to energy (F^r/E) are shown in Figure 4 together with the corresponding analytic solutions. The top panels plot the radiation energies, while the bottom panels are the radial flux ratios. The left (right) panels are the optically thinner (thicker) solutions. The qualitative behavior and results compare well to the solutions. We point out, as have previous authors (Smit et al. 1997; O'Connor 2015), that these tests are particularly sensitive to the closure relation, which helps to explain the deviations observed near the stellar surface. That our numerical methods can handle the discontinuities near the surface and match the asymptotic behavior extremely well is encouraging.

4.5. Doppler Frequency Shift

The frequency coupling terms from Section 3.2 are tested using the same series of calculations as performed by Müller et al. (2010), O'Connor (2015), and Kuroda et al. (2016). These tests involve the propagation of radiation from a homogeneous radiating sphere, similar to Section 4.4 except that in addition to isotropic absorption and emission, a sharp velocity profile is added outside the sphere to mimic an accretion flow capable of Doppler redshifting the outgoing radiation.

For all of these tests we set the stellar radius to $R_\star = 10$ km, and impose a uniform interior density of $\rho_0 = 9 \times 10^{14}\,\mathrm{g\,cm^{-3}}$ and temperature of $5\,\mathrm{MeV}/k$. The outer radius of the computational box is fixed at $R = 800$ km, and in order to resolve both the radiating sphere and Doppler velocity features we use 1080 cells along the radial direction, resulting in a grid resolution of $\Delta r = 0.74$ km. We choose to run these tests with neutrinos, rather than photons, and with both 15 and 25 frequency bins spanning the range 1–50 MeV/h. The stellar opacity is made sufficiently thick by setting the Péclet number to unity over the scale of a single zone. For the velocity profile we use

$$v(r) = \begin{cases} 0, & r \leqslant 70\ \mathrm{km}, \\ -0.2c\left(\frac{r - 70\ \mathrm{km}}{10\ \mathrm{km}}\right), & 70\ \mathrm{km} \leqslant r \leqslant 80\ \mathrm{km}, \\ -0.2c\left(\frac{80\ \mathrm{km}}{r}\right)^2, & r \geqslant 80\ \mathrm{km}. \end{cases} \tag{50}$$

In this section we consider tests of just the Doppler redshift arising from radiation streaming through the infalling velocity profile of Equation (50) without a gravitational potential. However, the same set of analytic solutions are equally applicable to cases with a redshifting potential as we will see in the next section. Variations in the luminosity arise in the free-streaming limit when there are nonzero velocities or potentials, and satisfy the following analytic solution

$$\mathcal{L}(r) \propto \frac{w}{\alpha}\frac{1-v}{1+v}\alpha r^2 g^{rr}\int F_r d\nu \propto \frac{w}{\alpha}\frac{1-v}{1+v}, \tag{51}$$

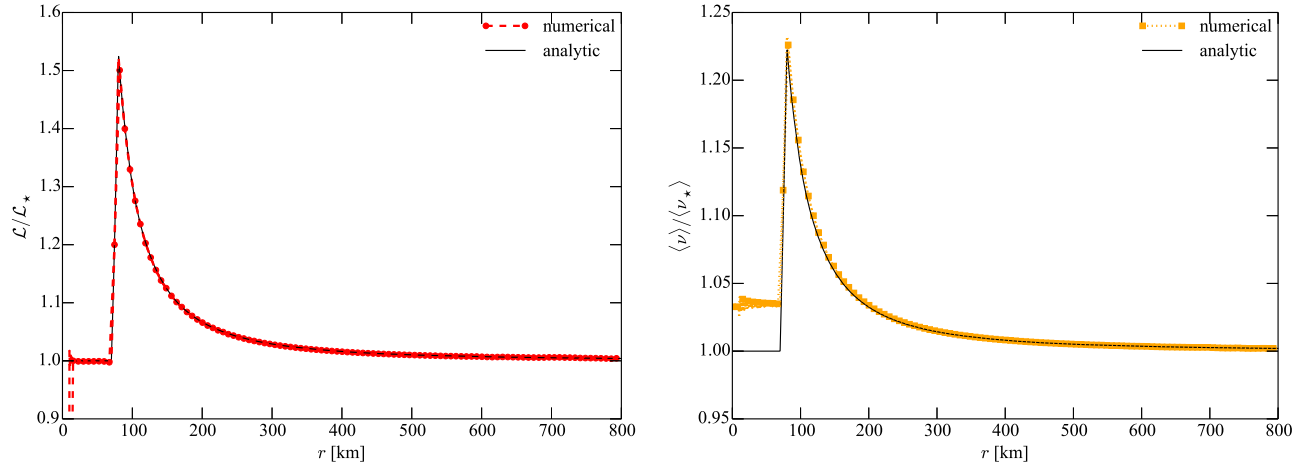

Figure 5. Steady-state luminosity (left) and mean co-moving neutrino energy (right) as functions of radius for neutrino streams undergoing Doppler redshifting from an accretion velocity field.

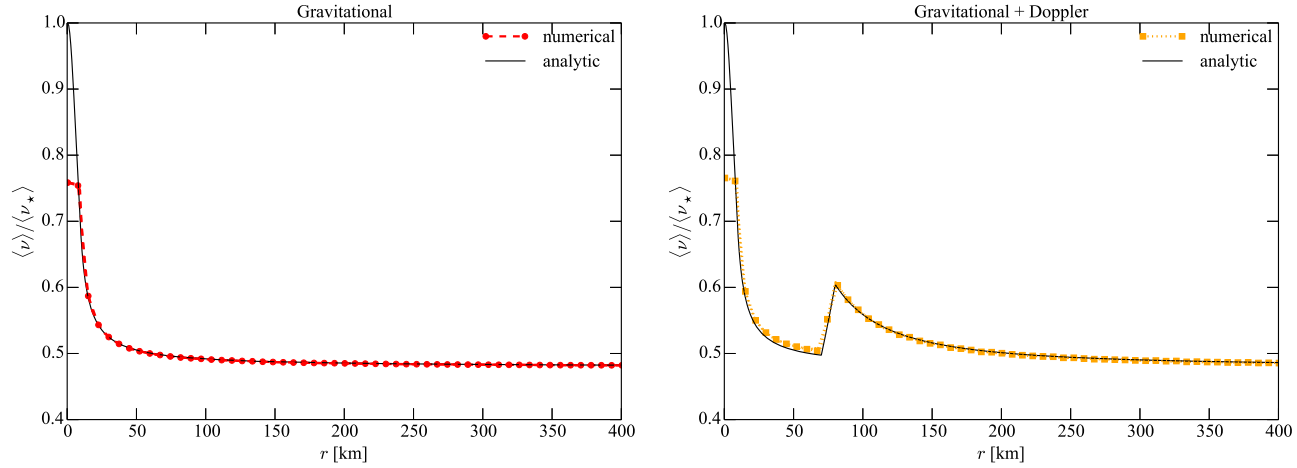

Figure 6. Mean co-moving neutrino energy as a function of radius for tests of pure gravitational (left) and gravitational plus Doppler (right) redshift.

where w is the Lorentz factor, $\alpha(r)$ is the lapse function, and the quantity $\alpha r^2 g^{rr} \int F_r d\nu$ is the luminosity measured by an Eulerian observer and should be constant far from the star. This implies that the mean neutrino energy as measured in the co-moving frame can be calculated as a function of radius:

$$h\langle\nu\rangle(r) = \frac{\alpha(R_\star)}{\alpha(r)} \frac{h\langle\nu_\star\rangle}{w(1+v(r))} \tag{52}$$

for both Doppler and gravitational redshifts provided the fluid velocity is zero at the star surface and $h\langle\nu_\star\rangle = 15.76\,\mathrm{MeV}$ is the mean neutrino energy at the stellar surface. Because of the high stellar opacity we can assume that any escaping radiation originates from the stellar surface $r = R_\star$.

Figure 5 shows the luminosity profile and the mean energy in the co-moving frame as functions of radius calculated with 25 frequency bins after the radiation achieves a steady state. The corresponding analytic solutions, also plotted in Figure 5, match the numerical results almost exactly everywhere except near the stellar surface, where the maximum error in the average photon energy (in the right plot) plateaus at about 3%. However, we point out that the width of the frequency bins near the emission frequency ($\nu_\star$) is $\delta\nu_n \approx 2\,\mathrm{MeV}/h$, or about $0.13\nu_\star$. Hence the observed error is within the uncertainty of interpolation between frequency bins, and convergences to zero with increasing frequency resolution, a fact that we have confirmed by running this identical test with a smaller number of frequency bins (15). We note that we importantly observe between first- and second-order convergence in matching the mean energies at the peak and in the region between the stellar surface and the velocity discontinuity. In particular the maximum errors with 15 (25) frequency bins in the near-surface plateau and Doppler peak regions are 5.3% (3.0%) and 1.6% (0.73%), respectively, corresponding to a convergence rate in frequency of about 1.5.

4.6. Gravitational Redshift

The problem from the previous section can readily be amended to test gravitational redshifting, too, which we do now. Aside from introducing a self-gravitating potential, all of the problem parameters and the configuration are identical to those specified previously. The potential ($\phi < 0$) is calculated by solving the Newtonian Poisson equation for the uniform-density sphere, then assigning the spacetime metric in the spherical, Kerr–Schild gauge as

$$ds^2 = -(1 + 2\phi/c^2)dt^2 + (1 - 2\phi/c^2)dr^2 + r^2 d\Omega^2. \tag{53}$$

Figure 6 displays the mean neutrino energy as a function of radius for two cases: pure gravitational redshift (left) and a combination of gravitational plus Doppler redshift with the

Table 1
Radiation Shock Tube Parameters

Case	Γ	κ^a	ρ_L	P_L	u^x_L	E_L	ρ_R	P_R	u^x_R	E_R
1	5/3	0.4	1	3×10^{-5}	0.0015	1×10^{-8}	2.4	1.61×10^{-4}	6.25×10^{-3}	2.51×10^{-7}
2	5/3	0.2	1	4×10^{-3}	0.25	2×10^{-5}	3.11	0.04512	0.0804	3.46×10^{-3}
3	2	0.3	1	60	10	2	8	2.34×10^{3}	1.25	1.14×10^{3}
4	5/3	0.08	1	6×10^{-3}	0.69	0.18	3.65	3.59×10^{-2}	0.189	1.30

same velocity profile as specified in Section 4.5 (right). Following the example in that section, we have run each scenario with 15 and 25 frequency bins to verify convergence. The solutions presented in Figure 6 are from the 25-bin tests. The Doppler peaks agree with the analytic solution to better than 1% for both resolutions. As found for the pure Doppler test, agreement is worst right in front of the velocity discontinuity. This region is sensitive to both the spatial and frequency resolutions. Our results with 15 (25) bins nevertheless agree with the analytic solution with maximum errors of about 3.1% (1.5%), converging between first and second order in frequency.

4.7. Radiation Shock Tube

Most of the tests we consider in this work do not involve both strong kinetic and thermal coupling between the radiation and matter. To address this, we include the following four radiation shock tube tests, first introduced by Farris et al. (2008) (see also Zanotti et al. 2011; Fragile et al. 2012; McKinney et al. 2014): a nonrelativistic strong shock (case 1), a relativistic strong shock (case 2), a relativistic wave (case 3), and a radiation pressure-dominated relativistic wave (case 4). The initial parameters are the same as those in Farris et al. (2008) and are reproduced in Table 1. These tests are run until $t = 300$ on a grid with 800 zones over $x \in [-20, 20]$. All calculations are run with spectrally uniform energy distributions, $E_{(\nu)n} = [E/(h\delta\nu_n)]/N_b$, and 18 frequency groups with bin edges at $0.05kT_{\rm min}/h$ and $20kT_{\rm max}/h$, where $T_{\rm min}$ and $T_{\rm max}$ come from the initial states of each case. The results are plotted in Figure 7, where we show (from top to bottom) the gas density, gas pressure, gas velocity, conserved radiation energy, and radiation rest-frame velocity for each case. We point out that we solve these problems using the $\boldsymbol{M}_1$ closure, whereas in most earlier work presenting these tests (e.g., Farris et al. 2008; Fragile et al. 2012, 2014; Sądowski et al. 2013), they were solved using the Eddington closure. Not surprisingly, the two closures yield slightly different results, which explains why our new results look different from our previously published ones (we also ran most of the cases to different stop times than before). Only one work that we are aware of, McKinney et al. (2014), has previously published these tests using the $\boldsymbol{M}_1$ closure, so our results should be compared with those, and in fact we find the agreement to be excellent.

4.8. Shadow Casting

An important advantage of $\boldsymbol{M}_1$ closure over the diffusion (or isotropic Eddington) approximation is its ability to preserve shadows in the wake of opaque objects. In a previous paper (Fragile et al. 2014) we demonstrated this ability with our gray (single group) version of $\boldsymbol{M}_1$. In that paper we considered radiation flow across an opaque spheroidal cloud embedded in a low-density transparent medium with a light source placed at one end of the computational domain. Here we generalize that test problem by replacing the spheroidal cloud with a density-stratified slab. As we will demonstrate, density stratification serves to exercise the multi-frequency capabilities of our new transport algorithm.

Four density layers are utilized in this test, along with three frequency groups. The background (transparent medium) density is fixed at 10^{-3} g cm^{-3}, while the opaque object is layered (from the bottom up) with densities of 10^3, 10^2, and 10 g cm^{-3}. The opaque slab is 1 cm long by 1 cm tall and rests 0.5 cm along the bottom of a grid $L = 3$ cm long by $4/3$ cm tall, resolved with 384×192 zones. Each density layer is $1/3$ cm thick. The gas and radiation begin in cold equilibrium with $T_{\rm gas} = T_{\rm rad} = 290$ K with a gas adiabatic index of $\Gamma = 5/3$. The photon streams are initialized at the left boundary with a uniform (frequency-integrated) source temperature $T_{\rm source} = 1740$ K, so that $E = a_R T^4$ and $F^x = 0.99999E$. Spectral energies and fluxes are initialized as $E_{(\nu)n} = [E/(h\delta\nu_n)]/N_b$ and $F_{(\nu)n} = cE_{(\nu)n}$, where $N_b = 3$ is the number of frequency bins.

The opacity of the gas is designed to produce the desired behavior of the bin-center energies through the different density layers. In particular, the frequency bin edges (2×10^{-3} and $2\,{\rm eV}/h$), the number of frequency groups (three, with logarithmic spacing), the opacity parameters, and the density layers are tailored so that each stacked layer of the slab is optically thin to a different frequency bin so that we can test shadow casting for each individual frequency group. This is accomplished with the following power law for absorption opacity (we do not consider scattering here):

$$\kappa^{\rm a} = \kappa_0 \left(\frac{\rho}{\rho_0}\right)^3 \left(\frac{\nu}{\nu_0}\right)^{-4} \ {\rm cm}^2\ {\rm g}^{-1}, \tag{54}$$

where the coefficient κ_0 is chosen to normalize the mean free path of the highest frequency photons through the densest (inner) layer to $\approx 10^{-2}$ cm, thus guaranteeing that the slab is sufficiently opaque in its bottom layer to block all streaming photons. Furthermore, the combination of densities and opacity power-law parameters defines essentially the same optical thickness to the middle frequency photons in the middle layer, and to the lowest frequency photons in the topmost layer.

From this configuration we expect to observe the following: all photons will be blocked by the bottom (highest density) layer; photons in the two lowest frequency bins will be blocked in the middle layer; only the lowest frequency photons will be blocked in the upper layer; and all photons will stream through the low-density gap above the opaque slab. Hence we should see a clear separation of photon streams and shadows if we plot each frequency bin separately. The results, after 1.5 light-crossing times, as shown in Figure 8, confirm these

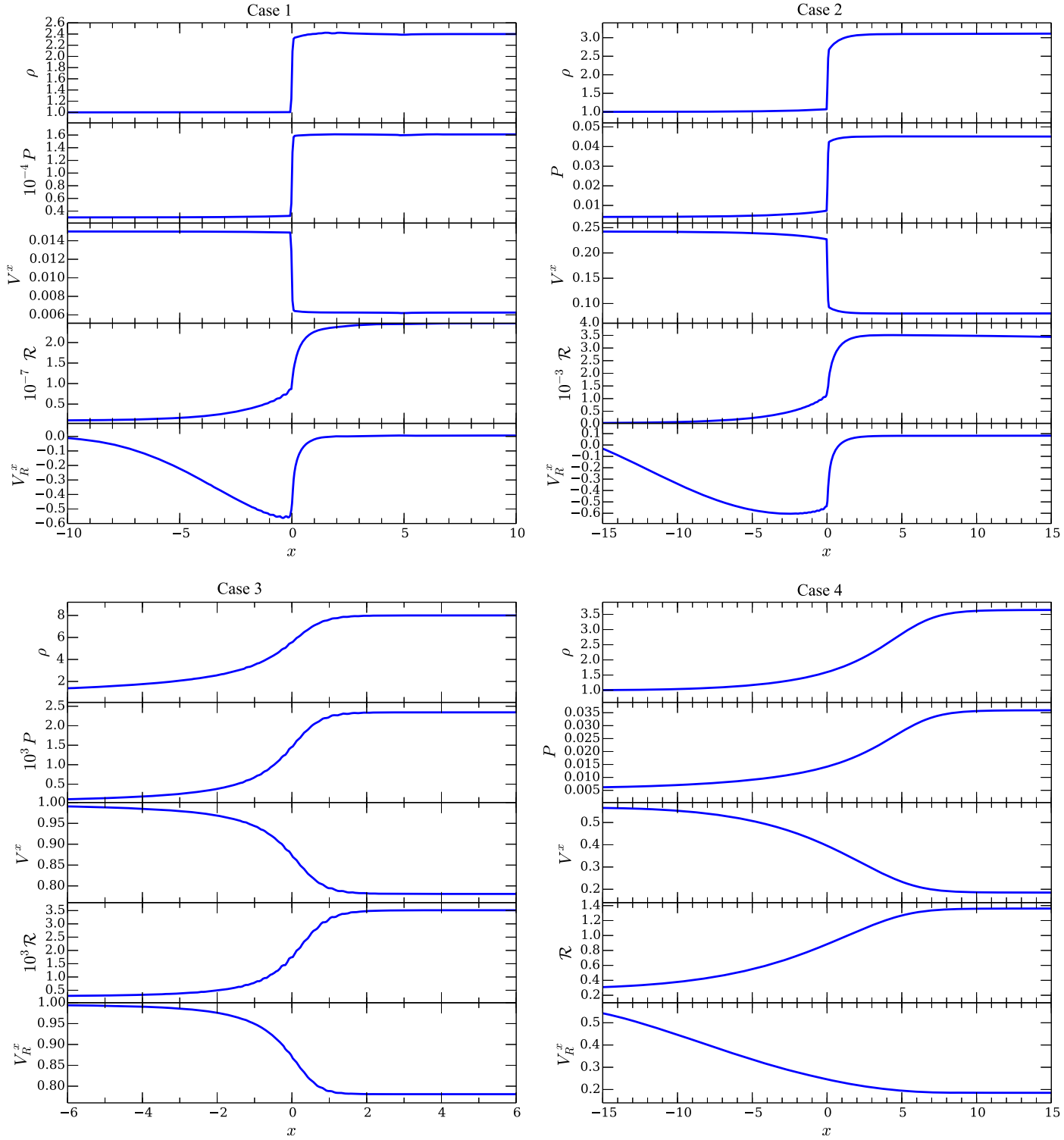

Figure 7. Profiles of gas density, gas pressure, gas velocity, conserved radiation energy, and radiation rest-frame velocity after $t = 300$ for the four radiation shock tube cases.

expectations. The three images plot $\mathcal{R}_{(\nu)n}$ for the center frequencies of the three photon bins, at roughly 0.01, 0.1, and 1 eV$/h$. As expected, the density layers produce sharp, clear shadows in both space and spectral energy. Notice that, as the radiation propagates, the edges of the shadows tend to flare out, a trait that is sensitive to the reconstruction method and limiter steepness (Davis et al. 2012; McKinney et al. 2014), yet the transition from light to dark is nevertheless quite pronounced at all frequencies. To demonstrate the clean separation of the three spectral components after passing through the stratified slab, we plot in Figure 9 the average photon energy as a function of the vertical height, y, crossing the horizontal position $x = 1.8$ cm. Also plotted is an "analytic" solution that is calculated by summing the energy only within the bin ranges that are theoretically transparent for a given height. The agreement is quite good.

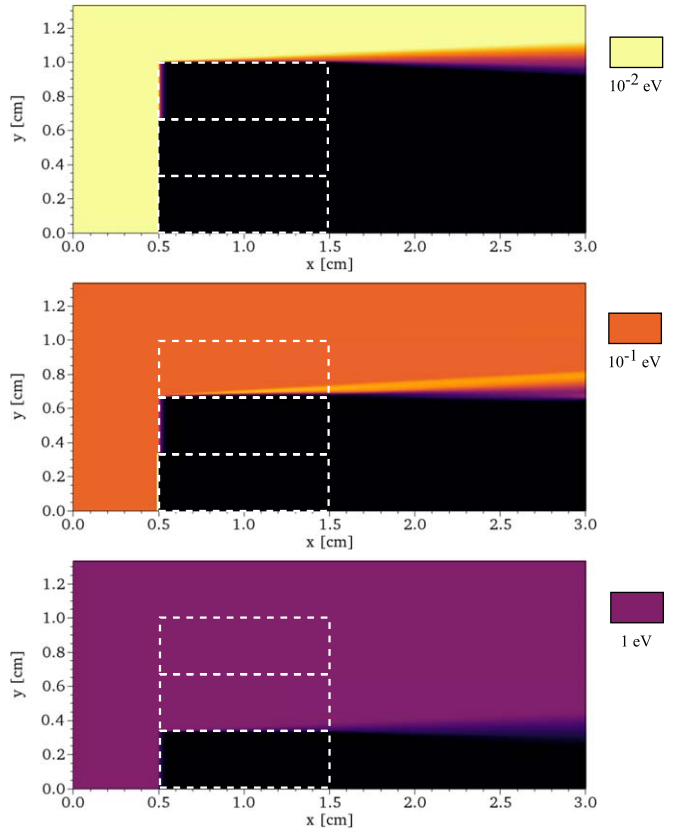

Figure 8. Pseudocolor plot of the conserved radiation spectral energy, $\mathcal{R}_{(\nu)n}$, for the multi-frequency shadow test. The bin-center energies, $h\nu_n$, increase from 10^{-2} eV (top image) to 10^{-1} eV (middle) to 1 eV (bottom). Colors are linearly scaled, using an independent normalization for each frame. The three different slabs (dashed, white lines) are constructed to be transparent at different frequencies.

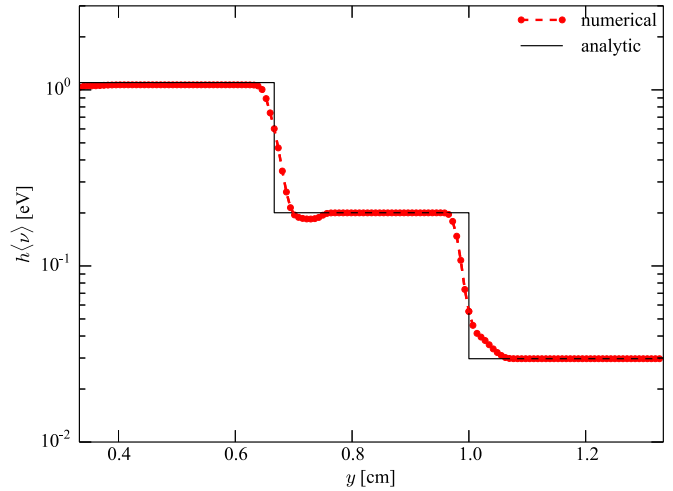

Figure 9. Line plot of the mean photon energy along the vertical (y) direction for all photons that cross position $x = 1.8$ cm in the multi-frequency slab shadowing problem. The first slab ($y < 1/3$ cm) is not shown since it is opaque to radiation. The black line is the expected photon energy calculated by only including source photons expected to be transmitted at a given height.

4.9. Two-beam Shadow Test

The shadow test from the previous section demonstrates one advantage of the $\boldsymbol{M}_1$ closure scheme over simpler flux-limited diffusion, the fact that it accurately casts shadows from a single beam incident upon an opaque object. However, a well-known shortcoming of flux-integrated (gray) $\boldsymbol{M}_1$ is that intersecting beams of light do not correctly cross one another. Instead, they merge, flowing in the direction of the average, resultant flux. A traditional illustration of this is the two-beam, shadow test (Sądowski et al. 2013; Fragile et al. 2014; McKinney et al. 2014). In this test, two beams of radiation enter the computational domain, one from the upper boundary and one from the lower. Each beam is angled toward a circular cloud along the centerline of the grid. Rather than the two beams casting two independent shadows as would be expected, they cast three partial shadows, one each in the directions of the original beams, and one in the "average" beam direction. This third shadow is the unphysical result of the partial merging of the two beams.

While our current multi-frequency $\boldsymbol{M}_1$ radiation transport does not provide a true solution to the issue of merging beams, it does admit an interesting workaround. Since photons (or beams) in different frequency bins are advected independently, and since there is no process in this test to trigger frequency exchanges, two beams of different frequencies can propagate independently, cross as expected, and cast individual shadows as they should. To illustrate this, we repeat the two-beam shadow test as presented in Sądowski et al. (2013) and Fragile et al. (2014), but with the new twist that each beam occupies a different frequency bin (the bin boundaries are not relevant). The test is run on a 120×120 grid, obviously with no reflection applied at $y = 0$. Figure 10 confirms our expectation that the two beams now leave only two shadows, one in each of the beam directions. Interestingly, since Figure 10 shows the frequency-integrated radiation energy and velocity, the beams *appear* to merge in the red triangular regions, but are actually still traveling in their independent directions.

4.10. Beam of Light Near a Black Hole

An important test for a general relativistic radiation transport scheme is to verify that the radiation propagates along geodesics as expected in strong gravitational fields. To verify this, we reproduce a series of light-beam tests introduced by Sądowski et al. (2013). For these tests we initialize a photon beam in the curved spacetime geometry near a $3M_\odot$ Schwarzschild black hole, and neglect any coupling interactions between the gas and radiation ($\kappa^a = \kappa^s = 0$) so that we can compare the path of the radiation beam against accurate geodesic paths. In this section, all distances are measured in units of GM/c^2. All calculations are run with five frequency groups covering 10–10^4 eV/h on a two-dimensional r–ϕ grid, with resolution 320×320 and grid coverage over $0 \leqslant \phi \leqslant \pi/2$ and $r_{\rm in} < r < r_{\rm out}$. We consider two cases: ($r_{\rm in}$, $r_{\rm out}$, $r_{\rm beam}$) = (2.5, 3.5, 3.0 ± 0.1) and (5.5, 11.5, 6 ± 0.2), where $r_{\rm beam}$ defines the beam center and width. Note that the beam in the first case is centered at the photon orbit radius, $r_{\rm beam} = r_{\rm p.o.} = 3$, meaning that photons in the center of the beam should be able to orbit the black hole indefinitely. The radiation temperature within the initial beam is $T_{\rm beam} = 10T_0 = 10^7$ K, where T_0 is the temperature of the background radiation. The radiation beam has an initial Lorentz factor of $\gamma = 10$ in the grid frame. The beam initial conditions are held constant at the $\phi = 0$ boundary.

Figure 11 shows the track of each radiation beam summed over all frequency bins, i.e., $R^0_0 = \int R^0_{0(\nu)}\, d\nu$, along with geodesic paths corresponding to the initial inner and outer boundaries of each beam. The left image corresponds to the photon orbit case with $r_{\rm beam} = 3$, while the right corresponds to

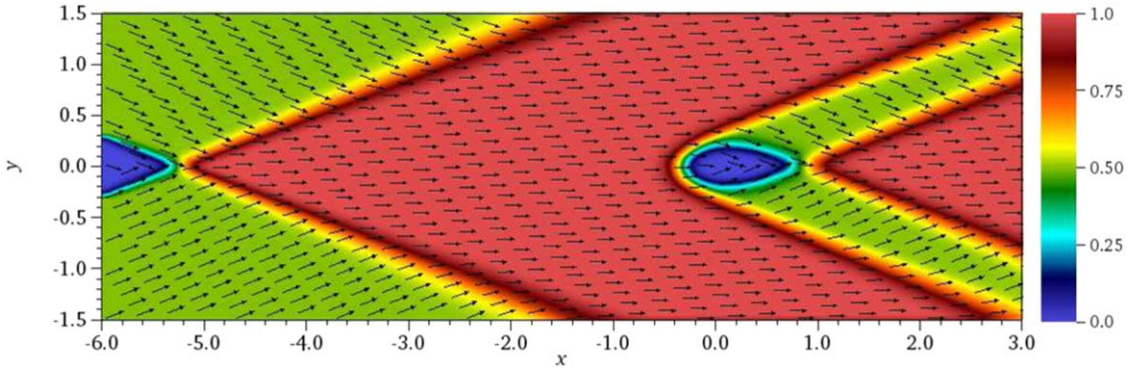

Figure 10. Pseudocolor plot of the frequency-integrated conserved radiation energy, $\mathcal{R}$, with vectors representing the radiation velocity, $u^i_{\rm R}$, for the two-beam cloud shadow test at $t = 20$. Note that the cloud casts two shadows, as it should.

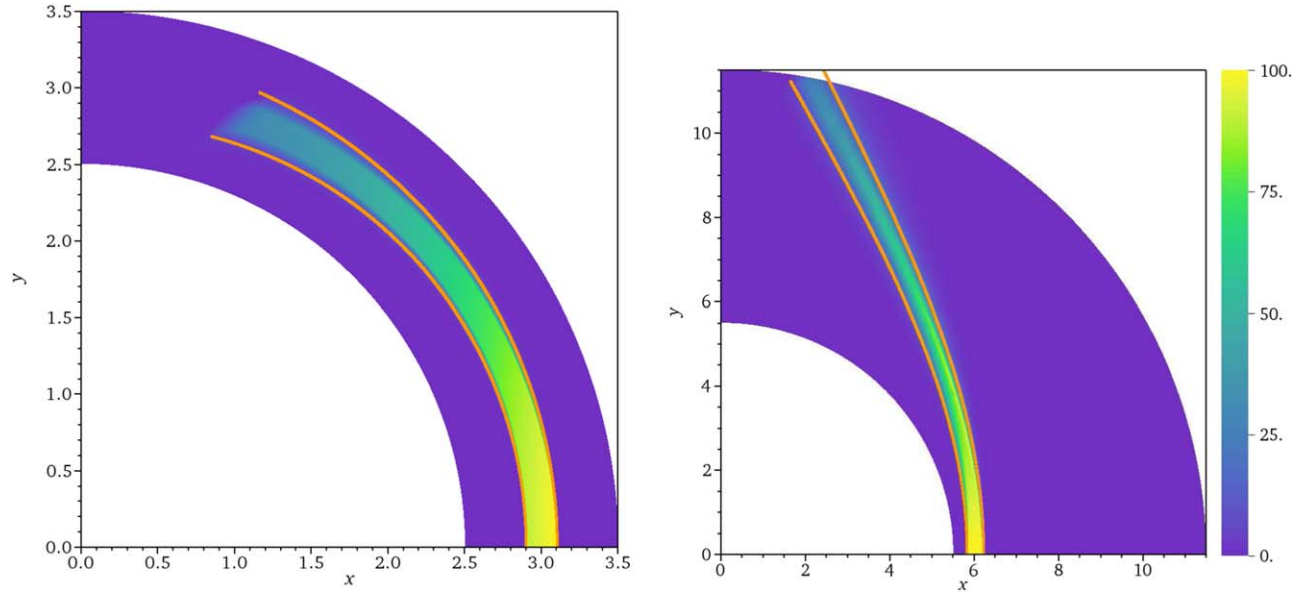

Figure 11. Pseudocolor image of the frequency-integrated conserved radiation energy, $R^0_0 = \int R^0_{0(\nu)}\, d\nu$, (in code units) for the light-beam tests. A Schwarzschild black hole is located at the coordinate origin. The light beams are introduced at the bottom boundary and propagate counterclockwise around the black hole. The orange curves represent geodesic paths starting at the initial inner and outer boundaries of the beam. Note that the background radiation energy is at least five orders of magnitude less than in the beam.

$r_{\rm beam} = 6$. We see that each beam stays confined within the prescribed geodesic tracks and experiences the expected curvature. Furthermore, each frequency group experiences the same curvature, so that the beam intensity is independent of the number of groups.

5. Conclusion

In this work, we have extended the capabilities of our *Cosmos++* computational astrophysics code to include multi-frequency radiation. This is done by selecting a finite number of frequency groups and independently evolving the radiation energy densities and momenta associated with each. We stick with the same explicit–implicit split of advection and radiation source terms and the two-moment $\boldsymbol{M}_1$ closure scheme as in our previous work (Fragile et al. 2014). Thus, we retain the ability to stably evolve a large range of parameter space from optically thin to optically thick flows with reasonable time steps and accuracy, while now relaxing the gray (frequency-integrated) approximation. In this work, we have focused on presenting and testing the general relativistic version, though we note that we have also implemented a Newtonian version as well. We also have a multi-group, flux-limited-diffusion option, which we plan to report on elsewhere.

This multi-frequency capability expands the range of physical processes that can be properly captured in a simulation. For example, we demonstrated how the new code could successfully treat frequency-dependent opacities and Doppler and gravitational frequency shifts, and to some extent overcome the multi-beam shadowing limitations of the $\boldsymbol{M}_1$ closure scheme.

While multi-frequency methods are already in use in studies of core-collapse supernovae (e.g., Just et al. 2015; Kuroda et al. 2016), they have many potential uses beyond that class of problem. Possible applications include Type Ia supernovae, neutron star mergers, tidal disruption events, and super-Eddington accretion onto compact objects. Another potential application is in the study of black hole X-ray binary accretion disks, especially in the so-called intermediate spectral states, where hard and soft X-ray photons each play important roles, not only in the observed spectra, but in physically interacting with the accretion flow, affecting its structure and thermodynamic state. It is important in such an application for hard and soft X-ray photons to be able to propagate independently,

experience the expected gravitational and Doppler frequency shifts, follow proper geodesic paths, and interact with the gas in a frequency-dependent manner—all of the capabilities we have demonstrated in this paper.

We thank the anonymous referee for their helpful comments and suggestions. The work by P.A. was performed under the auspices of the U.S. Department of Energy by Lawrence Livermore National Laboratory under Contract DE-AC52-AC52-07NA27344. P.C.F. gratefully acknowledges support from National Science Foundation grants AST-1616185 and AST-1907850. This work used the Extreme Science and Engineering Discovery Environment (XSEDE), which is supported by National Science Foundation grant number ACI-1053575.

Appendix
First-order Taylor Expansion Terms

The Jacobian matrix, $\boldsymbol{A}$, from Section 3.3 can be calculated either analytically or numerically. Although more tedious to code, we have found that the analytic method is consistently faster on all our tests, making it perhaps worth the extra effort. To aid those who might wish to code the analytic solution, we record all the pertinent partial derivatives for Equation (43) here, ordered by conserved field. Notice that we have dropped the frequency subscript notation in most of these expressions, but emphasize that radiation-related derivatives apply to all groups.

Mass density:

$$\frac{\partial D}{\partial \rho} = W$$
$$\frac{\partial D}{\partial u^i} = \sqrt{-g}\,\rho\frac{\partial u^0}{\partial u^i}$$
$$\frac{\partial D}{\partial \epsilon} = \frac{\partial D}{\partial E_R} = \frac{\partial D}{\partial u_R^i} = 0.$$

Fluid energy:

$$\frac{\partial \mathcal{E}}{\partial \rho} = -\sqrt{-g}\left[(1+\epsilon)u^0u_0 + (u^0u_0+1)\frac{\partial P_{\rm gas}}{\partial \rho}\right]$$
$$\frac{\partial \mathcal{E}}{\partial \epsilon} = -\sqrt{-g}\left[\rho u^0u_0 + (u^0u_0+1)\frac{\partial P_{\rm gas}}{\partial \epsilon}\right]$$
$$\frac{\partial \mathcal{E}}{\partial u^i} = -\sqrt{-g}\;(\rho+\rho\epsilon+P_{\rm gas})\left(u_0\frac{\partial u^0}{\partial u^i} + u^0\frac{\partial u_0}{\partial u^i}\right)$$
$$\frac{\partial \mathcal{E}}{dE_R} = \frac{\partial \mathcal{E}}{du_R^i} = 0.$$

Fluid momentum:

$$\frac{\partial \mathcal{S}_j}{\partial \rho} = \sqrt{-g}\;u^0u_j\left(1+\epsilon+\frac{\partial P_{\rm gas}}{\partial \rho}\right)$$
$$\frac{\partial \mathcal{S}_j}{\partial \epsilon} = \sqrt{-g}\;u^0u_j\left(\rho+\frac{\partial P_{\rm gas}}{\partial \epsilon}\right)$$
$$\frac{\partial \mathcal{S}_j}{\partial u^i} = \sqrt{-g}\;(\rho+\rho\epsilon+P_{\rm gas})\left(u_j\frac{\partial u^0}{\partial u^i} + u^0\frac{\partial u_j}{\partial u^i}\right)$$
$$\frac{\partial \mathcal{S}_j}{\partial E_R} = \frac{\partial \mathcal{S}_j}{\partial u_R^i} = 0.$$

Radiation energy:

$$\frac{\partial \mathcal{R}}{\partial E_R} = -\sqrt{-g}\left(\frac{4}{3}u_R^0(u_R)_0 + \frac{1}{3}\right)$$
$$\frac{\partial \mathcal{R}}{du_R^i} = -\frac{4}{3}\;\sqrt{-g}\,E_R\left((u_R)_0\frac{\partial u_R^0}{\partial u_R^i} + u_R^0\frac{\partial (u_R)_0}{\partial u_R^i}\right)$$
$$\frac{\partial \mathcal{R}}{\partial \rho} = \frac{\partial \mathcal{R}}{\partial \epsilon} = \frac{\partial \mathcal{R}}{\partial u^i} = 0.$$

Radiation momentum:

$$\frac{\partial \mathcal{R}_j}{\partial E_R} = \frac{4}{3}\;\sqrt{-g}\,u_R^0(u_R)_j$$
$$\frac{\partial \mathcal{R}_j}{\partial u_R^i} = \frac{4}{3}\;\sqrt{-g}\,E_R\left((u_R)_j\frac{\partial u_R^0}{\partial u_R^i} + u_R^0\frac{\partial (u_R)_j}{\partial u_R^i}\right)$$
$$\frac{\partial \mathcal{R}_j}{\partial \rho} = \frac{\partial \mathcal{R}_j}{\partial \epsilon} = \frac{\partial \mathcal{R}_j}{\partial u^i} = 0.$$

Also appearing in the Jacobian are the following gradients of the radiation 4-force density:

$$\frac{\partial G_\mu}{\partial \rho} = -(\kappa^{\rm a}+\kappa^{\rm s})R_{\mu\nu}u^\nu - (\kappa^{\rm s}R_{\alpha\beta}u^\alpha u^\beta + \kappa^{\rm a}B_{(\nu)})u_\mu$$
$$- \rho(R_{\mu\nu}u^\nu + B_{(\nu)}u_\mu)\frac{\partial \kappa^{\rm a}}{\partial \rho}$$
$$- \rho(R_{\mu\nu}u^\nu + R_{\alpha\beta}u^\alpha u^\beta u_\mu)\frac{\partial \kappa^{\rm s}}{\partial \rho}$$
$$- \rho\kappa^{\rm a}u_\mu\frac{dB_{(\nu)}}{dT}\frac{\partial T}{\partial \rho}$$
$$\frac{\partial G_\mu}{\partial \epsilon} = -\rho(R_{\mu\nu}u^\nu + B_{(\nu)}u_\mu)\frac{\partial \kappa^{\rm a}}{\partial \epsilon}$$
$$- \rho(R_{\mu\nu}u^\nu + R_{\alpha\beta}u^\alpha u^\beta u_\mu)\frac{\partial \kappa^{\rm s}}{\partial \epsilon}$$
$$- \rho\kappa^{\rm a}u_\mu\frac{dB_{(\nu)}}{dT}\frac{\partial T}{\partial \epsilon}$$
$$\frac{\partial G_\mu}{\partial u^i} = -\rho(\kappa^{\rm a}+\kappa^{\rm s})R_{\mu\nu}\frac{\partial u^\nu}{\partial u^i} - \rho(\kappa^{\rm s}R_{\alpha\beta}u^\alpha u^\beta + \kappa^{\rm a}B_{(\nu)})\frac{\partial u_\mu}{\partial u^i}$$
$$- \rho\kappa^{\rm s}u_\mu R_{\alpha\beta}\left(u^\alpha\frac{\partial u^\beta}{\partial u^i} + u^\beta\frac{\partial u^\alpha}{\partial u^i}\right)$$
$$\frac{\partial G_\mu}{\partial E_R} = -\rho(\kappa^{\rm a}+\kappa^{\rm s})u^\nu\frac{\partial R_{\mu\nu}}{\partial E_R} - \rho\kappa^{\rm s}u_\mu u^\alpha u^\beta\frac{\partial R_{\alpha\beta}}{\partial E_R}$$
$$\frac{\partial G_\mu}{\partial u_R^i} = -\rho(\kappa^{\rm a}+\kappa^{\rm s})u^\nu\frac{\partial R_{\mu\nu}}{\partial u_R^i} - \rho\kappa^{\rm s}u_\mu u^\alpha u^\beta\frac{\partial R_{\alpha\beta}}{\partial u_R^i}.$$

Finally, the following partial derivatives are needed to evaluate the above expressions:

$$\frac{\partial u_\alpha}{\partial u^i} = g_{0\alpha}\frac{\partial u^0}{\partial u^i} + g_{i\alpha}$$
$$\frac{\partial (u_R)_\alpha}{\partial u_R^i} = g_{0\alpha}\frac{\partial u_R^0}{\partial u_R^i} + g_{i\alpha}$$
$$\frac{\partial R_{\alpha\beta}}{\partial E_R} = \frac{4}{3}(u_R)_\alpha(u_R)_\beta + \frac{1}{3}g_{\alpha\beta}$$
$$\frac{\partial R_{\alpha\beta}}{\partial u_R^i} = \frac{4}{3}\;E_R\left[(u_R)_\alpha\frac{\partial (u_R)_\beta}{\partial u_R^i} + (u_r)_\beta\frac{\partial (u_R)_\alpha}{\partial u_R^i}\right].$$

ORCID iDs

P. Chris Fragile https://orcid.org/0000-0002-5786-186X

References

Aartsen, M. G., Ackermann, M., Adams, J., et al. 2019, arXiv:1911.02561
Abbott, B. P., Abbott, R., Abbott, T. D., et al. 2017, ApJL, 848, L12
Abbott, B. P., Abbott, R., Abbott, T. D., et al. 2018, LRR, 21, 3
Abdikamalov, E., Burrows, A., Ott, C. D., et al. 2012, ApJ, 755, 111
Abramowicz, M. A., & Fragile, P. C. 2013, LRR, 16, 1
Anninos, P., Bryant, C., Fragile, P. C., et al. 2017, ApJS, 231, 17
Anninos, P., Fragile, P. C., & Salmonson, J. D. 2005, ApJ, 635, 723
Burke-Spolaor, S. 2018, NatAs, 2, 845
Burns, E., Goldstein, A., Hui, C. M., et al. 2019, ApJ, 871, 90
Burrows, A. 2013, RvMP, 85, 245
Cerenkov Telescope Array Consortium, Acharya, B. S., Agudo, I., et al. 2019, Science with the Cerenkov Telescope Array (Singapore: World Scientific)
Chambers, K. C., Magnier, E. A., Metcalfe, N., et al. 2016, arXiv:1612.05560
Charles, P., & Shaw, A. 2013, A&G, 54, 6
Dai, L., McKinney, J. C., Roth, N., Ramirez-Ruiz, E., & Miller, M. C. 2018, ApJL, 859, L20
Davis, S. W., & Gammie, C. F. 2020, ApJ, 888, 94
Davis, S. W., Stone, J. M., & Jiang, Y.-F. 2012, ApJS, 199, 9
Dubroca, B., & Feugeas, J. 1999, CRASM, 329, 915
Fang, K., Metzger, B. D., Murase, K., Bartos, I., & Kotera, K. 2019, ApJ, 878, 34
Farris, B. D., Li, T. K., Liu, Y. T., & Shapiro, S. L. 2008, PhRvD, 78, 024023
Foglizzo, T., Kazeroni, R., Guilet, J., et al. 2015, PASA, 32, e009
Foucart, F., Haas, R., Duez, M. D., et al. 2016a, PhRvD, 93, 044019
Foucart, F., O'Connor, E., Roberts, L., et al. 2015, PhRvD, 91, 124021
Foucart, F., O'Connor, E., Roberts, L., et al. 2016b, PhRvD, 94, 123016
Fragile, P. C., Ballantyne, D. R., & Blankenship, A. 2020, NatAs, 6, 541
Fragile, P. C., Ballantyne, D. R., Maccarone, T. J., & Witry, J. W. L. 2018a, ApJL, 867, L28
Fragile, P. C., Etheridge, S. M., Anninos, P., Mishra, B., & Kluźniak, W. 2018b, ApJ, 857, 1
Fragile, P. C., Gillespie, A., Monahan, T., Rodriguez, M., & Anninos, P. 2012, ApJS, 201, 9
Fragile, P. C., Olejar, A., & Anninos, P. 2014, ApJ, 796, 22
Gammie, C. F., McKinney, J. C., & Tóth, G. 2003, ApJ, 589, 444
González, M., Audit, E., & Huynh, P. 2007, A&A, 464, 429
González, M., Vaytet, N., Commerçon, B., & Masson, J. 2015, A&A, 578, A12
Graham, M. J., Kulkarni, S. R., Bellm, E. C., et al. 2019, PASP, 131, 078001
IceCube Collaboration, Aartsen, M. G., Ackermann, M., et al. 2018, Sci, 361, eaat1378
Ivezić, Ž., Kahn, S. M., Tyson, J. A., et al. 2019, ApJ, 873, 111
Janka, H.-T. 2012, ARNPS, 62, 407
Jiang, Y.-F., Stone, J. M., & Davis, S. W. 2012, ApJS, 199, 14
Just, O., Obergaulinger, M., & Janka, H. T. 2015, MNRAS, 453, 3386
Keivani, A., Murase, K., Petropoulou, M., et al. 2018, ApJ, 864, 84
Kuroda, T., Takiwaki, T., & Kotake, K. 2016, ApJS, 222, 20
Lentz, E. J., Mezzacappa, A., Bronson Messer, O. E., et al. 2012, ApJ, 747, 73
Levermore, C. D. 1984, JQSRT, 31, 149
Levermore, C. D., & Pomraning, G. C. 1981, ApJ, 248, 321
McKinney, J. C., Tchekhovskoy, A., Sadowski, A., & Narayan, R. 2014, MNRAS, 441, 3177
Metzger, B. D. 2017, arXiv:1710.05931
Mishra, B., Fragile, P. C., Johnson, L. C., & Kluźniak, W. 2016, MNRAS, 463, 3437
Müller, B., Janka, H.-T., & Dimmelmeier, H. 2010, ApJS, 189, 104
O'Connor, E. 2015, ApJS, 219, 24
Pareschi, L., & Russo, G. 2001, Recent Trends in Numerical Analysis, Vol. 3 (Hauppauge, NY: Nova Scientific)
Pomraning, G. C. 1981, JQSRT, 26, 385
Pons, J. A., Ibanez, J. M., & Miralles, J. A. 2000, MNRAS, 317, 550
Ryan, B. R., & Dolence, J. C. 2020, ApJ, 891, 118
Sądowski, A., Narayan, R., Tchekhovskoy, A., & Zhu, Y. 2013, MNRAS, 429, 3533
Sekiguchi, Y., Kiuchi, K., Kyutoku, K., Shibata, M., & Taniguchi, K. 2016, PhRvD, 93, 124046
Senno, N., Murase, K., & Mészáros, P. 2017, ApJ, 838, 3
Shibata, M., Kiuchi, K., Sekiguchi, Y., & Suwa, Y. 2011, PThPh, 125, 1255
Skinner, M. A., Dolence, J. C., Burrows, A., Radice, D., & Vartanyan, D. 2019, ApJS, 241, 7
Smit, J. M., Cernohorsky, J., & Dullemond, C. P. 1997, A&A, 325, 203
Su, B., & Olson, G. L. 1999, JQSRT, 62, 279
Takahashi, H. R., Ohsuga, K., Kawashima, T., & Sekiguchi, Y. 2016, ApJ, 826, 23
Thorne, K. S. 1981, MNRAS, 194, 439
Tominaga, N., Shibata, S., & Blinnikov, S. I. 2015, ApJS, 219, 38
Wang, M.-H., Ai, S.-K., Li, Z.-X., et al. 2020, ApJL, 891, L39
Weih, L. R., Olivares, H., & Rezzolla, L. 2020, MNRAS, 495, 2285
Zanotti, O., Roedig, C., Rezzolla, L., & Del Zanna, L. 2011, MNRAS, 417, 2899
Zhang, W., Howell, L., Almgren, A., et al. 2013, ApJS, 204, 7